JEM Journal of Experimental Medicine

ARTICLE

Talin1 controls dendritic cell activation by regulating TLR complex assembly and signaling

Thomas Jun Feng Lim[1], Maegan Bunjamin[1], Christiane Ruedl[2], and I-hsin Su[1]

Talin critically controls integrin-dependent cell migration, but its regulatory role in skin dendritic cells (DCs) during inflammatory responses has not been investigated. Here, we show that talin1 regulates not only integrin-dependent Langerhans cell (LC) migration, but also MyD88-dependent Toll-like receptor (TLR)–stimulated DC activation. Talin1-deficient LCs failed to exit the epidermis, resulting in reduced LC migration to skin-draining lymph nodes (sdLNs) and defective skin tolerance induction, while talin1-deficient dermal DCs unexpectedly accumulated in the dermis despite their actomyosin-dependent migratory capabilities. Furthermore, talin1-deficient DCs exhibited compromised chemotaxis, NFκB activation, and proinflammatory cytokine production. Mechanistically, talin1 was required for the formation of preassembled TLR complexes in DCs at steady state via direct interaction with MyD88 and PIP5K. Local production of PIP2 by PIP5K then recruited TIRAP to the preassembled complexes, which were required for TLR signalosome assembly during DC activation. Thus, talin1 regulates MyD88-dependent TLR signaling pathways in DCs through a novel mechanism with implications for antimicrobial and inflammatory immune responses.

Introduction

Phagocytes, such as dendritic cells (DCs) and macrophages, sense pathogens through various pattern recognition receptors (PRRs) but exert distinct effector functions (Eisenbarth, 2019; Kaplan, 2017; Malissen et al., 2014; Merad et al., 2008). In contrast to the direct destruction of phagocytosed microbes by macrophages, pathogens phagocytosed by DCs are processed and effectively used for T cell priming (Eisenbarth, 2019; Malissen et al., 2014; Merad et al., 2008). The ability of DCs to regulate immunity is strictly dependent on their maturation and activation state (Eisenbarth, 2019; Malissen et al., 2014; Worbs et al., 2017). Microbe recognition via PRRs activates and induces the maturation of DCs, which not only promotes their migratory ability to deliver pathogen-derived antigens to immune cells in nearby lymphoid organs, but also greatly enhances their T cell stimulatory capacity by up-regulating MHC and costimulatory molecules (Malissen et al., 2014). TLRs are perhaps the best characterized PRRs (Gay et al., 2014; Kawasaki and Kawai, 2014; O'Neill and Bowie, 2007). Ligand binding to various TLRs either induces receptor dimerization or alters the conformation of preexisting dimers (Gay et al., 2014; Park et al., 2009), thereby triggering distinct signaling pathways involving two adaptor molecules, myeloid differentiation primary response protein 88 (MyD88) and TIR domain–containing adapter-inducing interferon-β (TRIF), to promote NFκB or IRF3/7 activation and proinflammatory cytokine production (Gay et al., 2014; Kawasaki and Kawai, 2014; O'Neill and Bowie, 2007). Notably, all TLRs require the engagement of MyD88 to initiate downstream signaling pathways with the exception of TLR3, which only uses only TRIF (Gay et al., 2014; Kawasaki and Kawai, 2014; O'Neill and Bowie, 2007).

Mature DCs are fast migrating cells that are able to move through various tissues by switching between different migration modes (Lämmermann et al., 2008; Renkawitz et al., 2009; Worbs et al., 2017). For instance, following cutaneous insults, epidermal DCs called Langerhans cells (LCs) up-regulate α6 integrin (Price et al., 1997) to enable passage across the basement membrane into the dermis while concomitantly up-regulating chemokine receptors CXCR4 and CCR7 to promote migration to the skin-draining lymph nodes (sdLNs; Kabashima et al., 2007; Ohl et al., 2004). Whereas transmigration across the basement membrane is an integrin-dependent process (Gunawan et al., 2015; Loh et al., 2018; Worbs et al., 2017), the movement of migratory LCs (mLCs) or dermal DCs (mdDCs) from the dermis to sdLNs via interstitial tissues and lymphatic vessels is mainly achieved by integrin-independent actomyosin contractions (Loh et al., 2018; Worbs et al., 2017). Talin, a key adaptor molecule of

[1]Laboratory of Molecular Immunology & Cell Signalling, School of Biological Sciences, College of Science, Nanyang Technological University, Singapore, Republic of Singapore; [2]Laboratory of Immunology, School of Biological Sciences, College of Science, Nanyang Technological University, Singapore, Republic of Singapore.

Correspondence to I-hsin Su: ihsu@ntu.edu.sg; Thomas Jun Feng Lim: thomasjf.lim@ntu.edu.sg.

integrin signaling, is required for integrin-dependent cell adhesion and migration, but not actomyosin contractility-driven cell migration (Calderwood et al., 2013; Lämmermann et al., 2008). Consistently, talin1-deficient B cells and T cells are defective in homing to LNs because of the failure of integrin-dependent extravasation from blood vessels (Manevich-Mendelson et al., 2010; Wernimont et al., 2011). A similar inability to migrate contributes to the defective infiltration of talin1-deficient neutrophils into the peritoneal cavity during peritonitis (Lim and Su, 2018; Yago et al., 2015).

Integrins are likely to have broader physiological roles in addition to their well-described functions in cell adhesion/migration and cell–cell contacts. Several atypical functions of integrins have been reported. For example, αvβ6 and αvβ8 integrins bind to and activate pro-TGF-β in a cytoskeletal force-dependent manner (Shi et al., 2011; Wang et al., 2017). However, alternative functions of talin, besides cell adhesion, have not been investigated. Here, we demonstrate for the first time that talin1 critically regulates DC activation by forming a preassembled TLR complex that is required for ligand-induced MyD88-dependent TLR signaling pathways. Talin1-deficient DCs showed compromised integrin-dependent and -independent migration as well as inflammatory cytokine production. Consequently, antimicrobial immune responses and tolerance induction against innocuous cutaneous allergen were compromised in mice with talin1-deficient DCs. Further molecular studies revealed that Talin1 links active integrins to TLRs via direct interaction with MyD88 while promoting TIR-domain containing adapter protein (TIRAP) recruitment by increasing local PIP2 concentration through interaction with PIP5K. In conclusion, we provide mechanistic insight into the novel mechanism of talin1-regulated TLR-mediated DC activation and migration both in vitro and in vivo.

Results

Talin1 regulates skin DC migration to sdLNs

Because the migration of LCs across the epidermal basement membrane is mediated by integrin α6β1 (Price et al., 1997), talin1 is likely to be essential for LC migration in vivo. To address the role of talin1 in LC migration, epidermal ear sheets were isolated from control (*Tln1*$^{f/f}$) and *Tln1*$^{f/f}$*CD11c*-Cre mice under steady state and stained for MHCII to visualize epidermal LCs. We observed significant increases in the numbers of talin1-deficient LCs found in ear tissues, compared with wild-type LCs (Fig. 1 A). This observed increase was not caused by enhanced cell proliferation, as determined by BrdU incorporation assays (Fig. S1 A). Moreover, an additional talin isoform, talin2 (*Tln2*), and the integrin coactivator kindlin3 (*Fermt3*) were not up-regulated, although the expressions of metalloproteinases MMP2 and 9 (*Mmp2/9*) were increased (Fig. S1 B). The number of talin1-deficient LCs also increased persistently during mild inflammation (painting of the nonallergic hapten 2,4-dinitrothiocyanobenzene [DNTB]) and under severe inflammatory conditions (intradermal [i.d.] injection of bacterial-derived LPS or ear explant culture; Larsen et al., 1990; Fig. 1 A). The total cell numbers of LCs in the epidermis, dermis, and sdLNs were further determined by cell counting and flow cytometric analyses. Consistent with the results from the epidermal sheet staining, talin1-deficient LCs accumulated in the epidermis, and consequently, the number of talin1-deficient mLCs in the dermis and sdLNs was reduced under steady state (Fig. 1, B–D) and upon LPS stimulation (Fig. 1 E). To determine whether the basement membrane is the physical barrier preventing the transmigration of talin1-deficient LCs into the dermis, we first subjected excised skin samples to dispase digestion to disrupt the integrity of the basement membrane and cultured the isolated epidermis to facilitate LC activation in vitro. Under these conditions, talin1-deficient LCs were able to migrate away from epidermal sheet explants (Fig. S1 C), supporting the idea that talin1 has a critical role in integrin-dependent LC transmigration across the basement membrane.

In addition to changes in talin1-deficient LC migration, we also noticed that talin1-deficient dDC subsets accumulated in the dermis (Fig. 1 C) and that corresponding reductions in mdDC numbers were observed in sdLNs under steady state (Fig. 1 D) and upon LPS treatment (Fig. 1 E), suggesting that the migration of talin1-deficient dDCs from the dermis to sdLNs was compromised. This result is rather unexpected, because DCs are known to be able to perform integrin-independent/actomyosin-dependent migration effectively in a 3D matrix (Lämmermann et al., 2008). To further investigate DC migration in vitro, we embedded wild-type and talin1-deficient bone marrow (BM)–derived DCs (BMDCs) from poly(I)•poly(C)-treated *Tln1*$^{f/f}$*Mx*-Cre mice in 3D collagen matrices (Fig. 1 F). BMDCs derived from poly(I)•poly(C)-treated *Tln1*$^{f/f}$*Mx*-Cre mice showed complete depletion of talin1 protein (Fig. S1 D). Our results revealed a significant reduction in the migratory capacity of talin1-deficient LPS-matured BMDCs upon chemokine (CCL19) stimulation, compared with that of wild-type cells, in a dose-dependent manner (Fig. 1 G and Fig. S1 E). However, up-regulation of the CCL19 receptor (CCR7; Fig. 1 H) and cell signaling capacities (Fig. 1, I and J) of BMDCs upon CCL19 stimulation were not affected by talin1 deficiency. These results suggest that talin1 controls the 3D migration of DCs both in vitro and in vivo, by as yet unidentified mechanisms.

Talin1 regulates DC activation

Down-regulation of surface E-cadherin coincides with epidermal LC mobilization/maturation in both steady state and during inflammation (Jakob and Udey, 1998; Jiang et al., 2007). Up-regulation of MHCII and the costimulatory molecule CD86 are also commonly used to study DC activation (Price et al., 2015). To identify differences in cell activation states in the absence of talin1, we examined the expression profiles of these surface activation markers in both control and talin1-deficient LCs in the absence and presence of inflammatory stimulation. The results of these studies showed that even though the surface expression levels of E-cadherin, MHCII, and CD86 of talin1-deficient and control LCs were comparable at steady state (Fig. 2 A) and both were able to up-regulate CCR7 and CXCR4 in 24-h skin explant cultures (Fig. S2 A), down-regulation of E-cadherin took place only on the surface of wild-type, but not talin1-deficient, LCs (Fig. 2 A). Because the total levels of E-cadherin were comparable between control and talin1-deficient LCs, the defective down-regulation of E-cadherin in talin1-deficient LCs was not

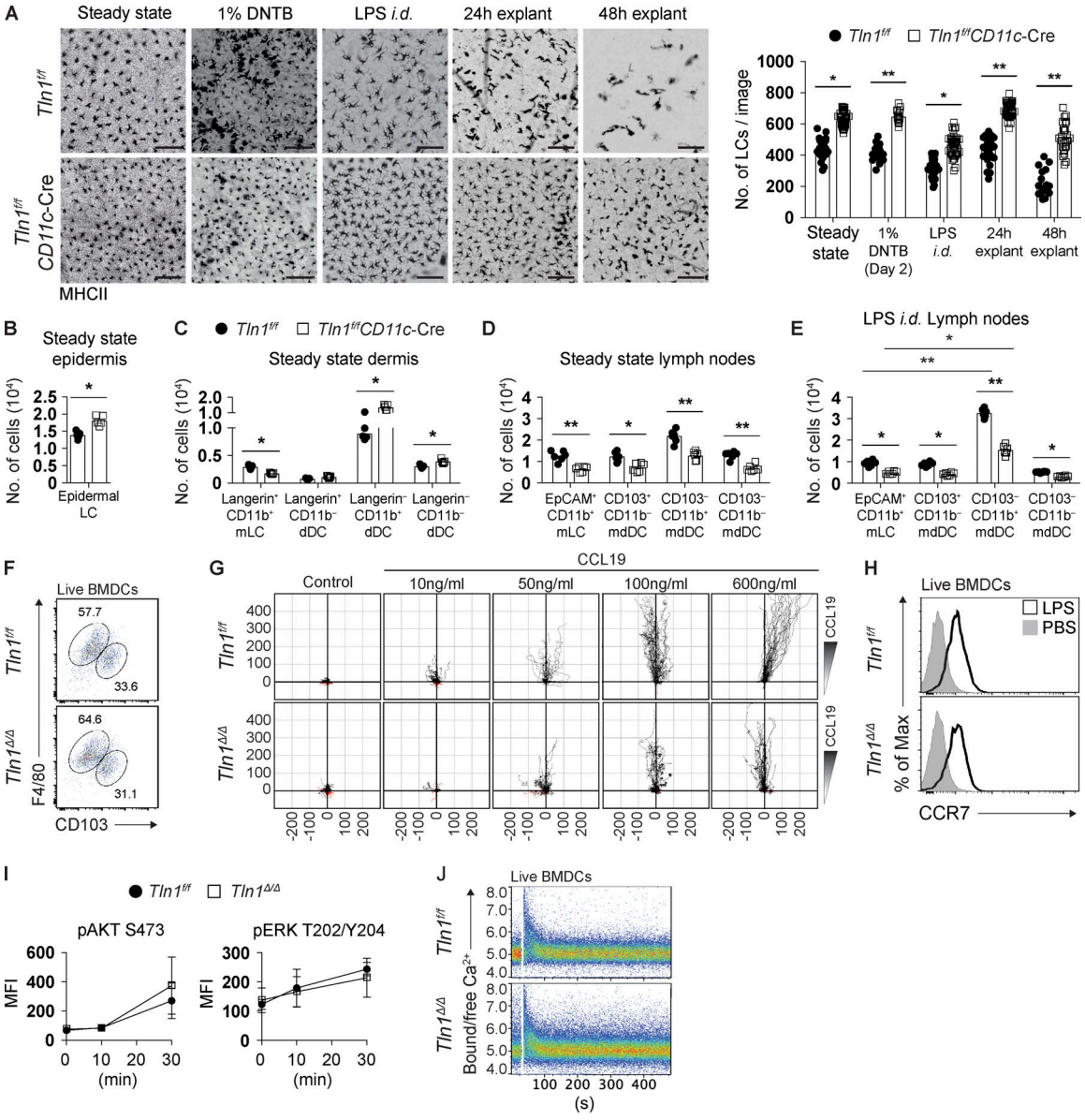

Figure 1. **Talin1-deficient skin DCs fail to migrate to sdLNs. (A)** Immunofluorescence analysis (left) and quantification (right) of LCs on epidermal ear sheets isolated from control (*Tln1*$^{f/f}$) and *Tln1*$^{f/f}$*CD11c*-Cre mice painted with 1% DNTB or i.d. injected with LPS, or explants cultured for 24 and 48 h. LCs were identified by MHCII staining. Five images/ear/mouse. Scale bars, 20 µm. *n* = 3–6 mice/group. **(B–E)** Absolute numbers (scatter plots) of DC subsets in epidermis (B), dermis (C), and sdLNs (D) of *Tln1*$^{f/f}$ control and *Tln1*$^{f/f}$*CD11c*-Cre mice under steady state or 48–60 h after i.d. LPS injection (E). *n* = 5–6 mice/group. **(F)** Flow cytometric analysis of BMDCs derived from BM cells of poly(I)•poly(C)-injected control (*Tln1*$^{f/f}$) and *Tln1*$^{f/f}$*Mx*-Cre mice cultured in the presence of GM-CSF. Surface expression of indicated markers on CD11c$^+$MHCII$^+$ DCs is shown. BMDCs generated from poly(I)•poly(C)-treated *Tln1*$^{f/f}$*Mx*-Cre mice are hereafter referred to as *Tln1*$^{\Delta/\Delta}$ BMDCs. **(G)** Cell tracks of wild-type and talin1-deficient BMDCs migrating toward CCL19. Black tracks, forward migration; red tracks, reverse migration. At least 30 control or *Tln1*$^{\Delta/\Delta}$ BMDCs were tracked per experiment. **(H)** Histograms of CCR7 expression levels in immature and LPS-matured BMDCs analyzed by flow cytometry. **(I and J)** Mean fluorescence intensities (MFIs) of phospho-AKT S473 (I, left) and phospho-ERK1/2 T202/Y204 (I, right), as well as pseudocolor plots of calcium flux (J) in LPS-matured control and talin1-deficient BMDCs upon CCL19 stimulation, as determined by flow cytometric analyses. Data were pregated on singlet, live cells (B–F and H–J). BMDCs were defined as CD11c$^+$MHCII$^+$ (F–J). Each point in the scatter bar graphs indicates the cell number from one image (A) or one mouse (B–E and J). Data are representative or summaries of three (F and H–J; mean ± SD) or three to five (A–E and G; mean ± SD) independent experiments. *, 0.01 < P ≤ 0.05; **, 0.005 < P ≤ 0.01 (two-tailed Student's *t* test).

due to intrinsic differences in E-cadherin expression (Fig. 2 A). Similarly, the expressions of CD86 and MHCII were substantially up-regulated in control LCs under various inflammatory conditions, such as explant culture (Fig. 2 A), i.d. LPS injection (Fig. S2 B), and treatment with the innocuous weak hapten 5,5′-dithiobis-2-nitrobenzoic acid (DNTB; Fig. S2 C), but remained unchanged or were weakly up-regulated in talin1-deficient LCs (Fig. 2 A and Fig. S2, B and C). These data suggest that talin1 is likely involved in regulating DC activation in general. Indeed, talin1-deficient dDCs (Fig. 2 B) and BMDCs (Fig. 2 C) exhibited similar defects in the up-regulation of activation markers (CD86 and MHCII) in explant culture and upon LPS stimulation, respectively.

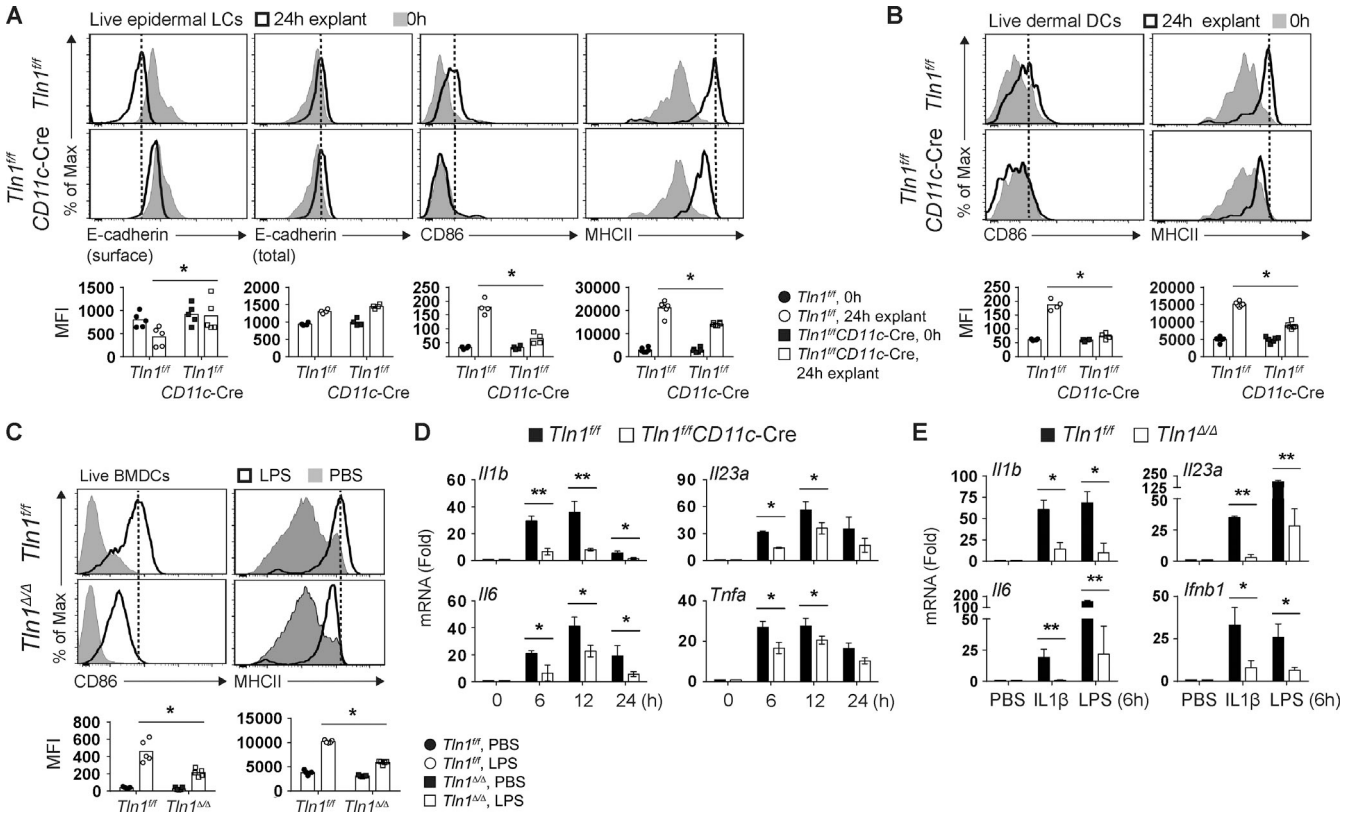

Figure 2. **Talin1 critically regulates DC activation upon LPS stimulation. (A and B)** Surface or total (intracellular and surface) expression levels of the indicated molecules in control (*Tln1*$^{f/f}$) and talin1-deficient (*Tln1*$^{f/f}$*CD11c*-Cre) LCs (A) or dermal DCs (B) isolated from untreated ear explants or ear explants cultured for 24 h, as determined by flow cytometry. Three independent experiments (n = 6 mice/group). **(C)** Flow cytometric analysis of the indicated molecules on the surface of wild-type and talin1-deficient (*Tln1*$^{\Delta/\Delta}$) BMDCs stimulated with LPS overnight. Dashed lines in A–C designate the peak position of indicated molecules expressed in control DCs upon activation. Bar chart below each histogram summarizes MFIs of respective molecules from different experiments (n = 4–5). **(D)** mRNA expression levels, as determined by RT-qPCR, of *Il1b*, *Il6*, *Il23a*, and *Tnfa* in FACS-sorted wild-type and talin1-deficient LCs isolated from untreated explants or explants cultured for 6, 12, or 24 h. Three independent experiments (n = 3 mice/group). **(E)** RT-qPCR results showing the mRNA expression levels of *Il1b*, *Il6*, *Il23a*, and *Ifnb1* in wild-type and talin1-deficient BMDCs stimulated with IL1β, TNFα, or LPS, as indicated, for 6 h. *Gapdh* was used as an internal control (D and E). BMDCs were generated from the BM cells of poly(I)•poly(C)-treated *Tln1*$^{f/f}$ and *Tln1*$^{f/f}$*Mx*-Cre mice, as described in Fig. 1 F. Data shown are representative or summaries of three independent experiments (mean ± SD). *, 0.01 < P ≤ 0.05; **, 0.005 < P ≤ 0.01; ***, P ≤ 0.005 (two-tailed Student's t test).

To investigate the consequences of talin1 deficiency in LC activation, we sorted wild-type and talin1-deficient epidermal LCs from cultured skin explants by FACS to determine the expression levels of proinflammatory cytokines. Consistently lower transcript levels of *Il1b*, *Il6*, *Il23a*, and *Tnfa* were detected in talin1-deficient LCs than in control LCs (Fig. 2 D). Similarly, reduced mRNA transcript and protein levels of proinflammatory cytokines, such as *Il1b*, *Il6*, *Il23a*, and *Ifnb1*, were detected in LPS- or IL-1β–stimulated talin1-deficient BMDCs, compared with wild-type BMDCs (Fig. 2 E and Fig. S2 D). Together, these data support our proposition that talin1 deficiency compromises the activation of LCs and BMDCs and justify the use of BMDCs as a tool to study the molecular mechanisms of talin1-regulated DC activation.

Talin1 promotes LPS-induced NFκB activation in DCs

Because NFκB is an important downstream effector of TLR signaling cascades and controls the expression of several of the proinflammatory cytokines examined above (Gay et al., 2014; Kawasaki and Kawai, 2014; Ling et al., 2014), we sought to determine whether talin1 deficiency affects NFκB activation in DCs. Our data revealed that NFκB activation, as determined by the nuclear translocation of p65 upon LPS stimulation, was significantly reduced in talin1-deficient BMDCs compared with control cells (Fig. 3 A), which correlated with decreased IκB phosphorylation and degradation (Fig. 3 B). In parallel, we also found that TLR4-associated phosphoinositide 3-kinase (PI3K) pathway activation was compromised in talin1-deficient DCs, as indicated by decreased AKT phosphorylation (Fig. 3 B). Furthermore, activation of the MAPK pathway was also modestly reduced in the absence of talin1, as determined by phospho-ERK1/2 and phospho-p38 immunoblotting studies (Fig. 3 B). However, JNK activation was not affected by talin1 deficiency (Fig. 3 B). To determine whether the observed signaling defects were specific to GM-CSF–derived BMDCs, we generated DCs from Flt3 ligand (Flt3L)–supplemented BM cultures and analyzed the signaling capacities of individual DC subsets (pDC, cDC1, and cDC2) by phosphor-flow cytometric analysis. The percentages of the various DC subsets derived from Flt3L- or GM-CSF–supplemented control and talin1-deficient BM cultures

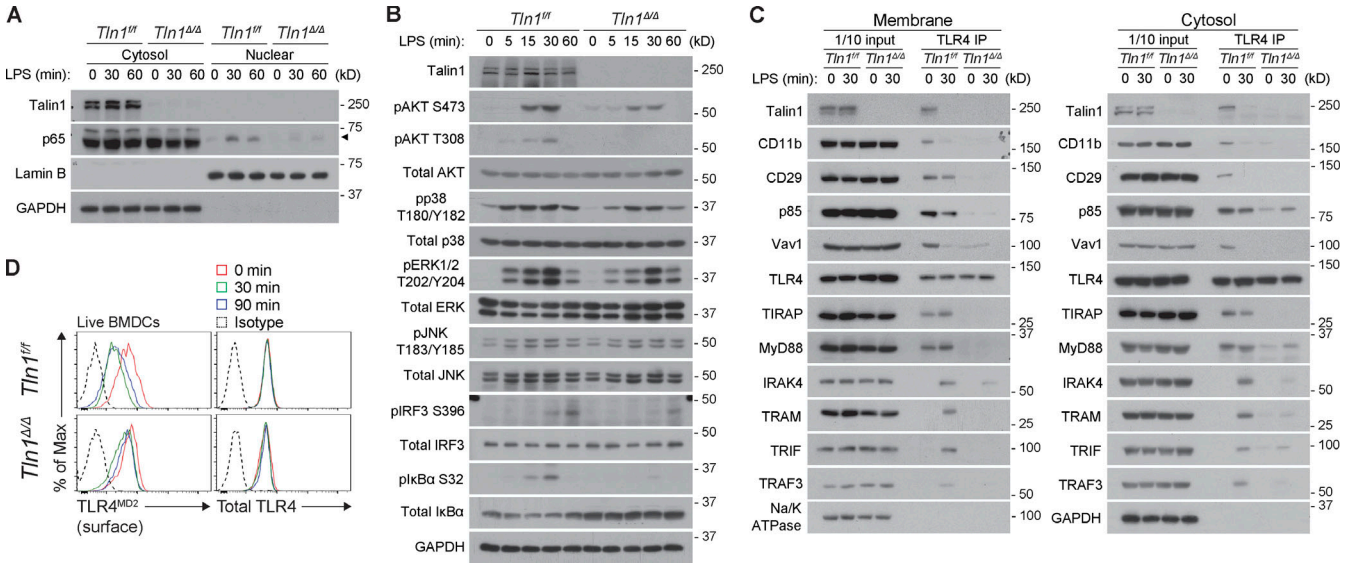

Figure 3. **Talin1 controls TLR4-mediated signaling cascades in DCs. (A and B)** Immunoblot analysis of the cytosolic and nuclear fractions (A) or total lysate (B) of control (*Tln1*$^{f/f}$) and talin1-deficient (*Tln1*$^{Δ/Δ}$) GM-CSF–derived BMDCs stimulated with LPS for the indicated times. **(C)** IP of TLR4 from the membrane (left) and cytosol (right) fractions of wild-type and talin1-deficient BMDCs stimulated with LPS, followed by immunoblot analysis for the indicated proteins. 10% (1 of 10) of the cell lysates used for IPs were run as input controls. **(D)** Flow cytometric analysis of surface TLR4 associated with MD2 (hereafter referred to as TLR4^{MD2}, left) or total TLR4 (intracellular and surface, right) in control and talin1-deficient BMDCs stimulated with LPS. Data were pregated on singlet, live BMDCs. GAPDH (total lysates and cytosolic fractions) and Na/K ATPase (membrane fractions) were used as loading controls. BMDCs were generated from the BM cells of poly(I)•poly(C)-treated *Tln1*$^{f/f}$ and *Tln1*$^{f/f}$*Mx*-Cre mice, as described in Fig. 1 F. Cells were pooled from two to three mice/group for each IP followed by immunoblot experiment. Data shown are representative of three independent experiments.

were comparable (Fig. S3, A and B). Notably, across the different DC subsets derived from each BM culture system, talin1-deficient cells consistently showed similar signaling defects upon LPS stimulation compared with control cells, as determined by the levels of phospho-ERK (T202/Y204) and phospho-AKT (S473; Fig. S3, C–F). The reduced activation of ERK and AKT in Flt3L-derived BMDCs was further confirmed by immunoblot analysis (Fig. S3 G). Collectively, our data indicate that talin1 is likely to control TLR4-mediated signaling pathways upstream of NFκB, thereby regulating the activation of the investigated DC subsets.

Talin1 is essential for preassembly of the TLR4 complex and LPS-induced signalosome assembly in DCs

Because LPS signaling through TLR4 induces the assembly of the Myddosome and the Triffosome (Gay et al., 2014; Lin et al., 2010), we propose that talin1 is involved in the assembly of these higher-order complexes. To address this question, we separated unstimulated and LPS-stimulated control and talin1-deficient BMDCs into cytosolic and membrane fractions and then performed immunoprecipitations (IPs) for TLR4. Upon LPS stimulation, components of the MyD88-dependent pathway, such as TIRAP, MyD88, IRAK4, and, sequentially, molecules unique to the TRIF-dependent pathway (TRAM, TRIF, and TRAF3) were recruited to TLR4 (both membrane bound and cytosolic) within the first 30 min of TLR4-LPS ligation in wild-type BMDCs (Fig. 3 C). Interestingly, we observed that talin1 associated with a preassembled TLR4 complex consisting of TLR4/TIRAP/MyD88 in unstimulated wild-type BMDCs and remained in this complex 10 min after LPS stimulation (Fig. S3 H). This preassembled TLR4/MyD88 complex was unique to both GM-CSF– and Flt3L-derived DCs (Fig. 3 C and Fig. S3, H and J), but was not detected in BM-derived macrophages (BMDMs; Fig. S4, A and B). Moreover, the preassembled complex observed in control DCs also associated with several regulatory molecules such as p85 (the regulatory subunit of the PI3K complex), Vav1-guanine nucleotide exchange factor, CD11b (integrin αM), and CD29 (integrin β1; Fig. 3 C and Fig. S3 H). Similar to talin1, most of these regulatory molecules were still associated with TLR4 10 min after LPS stimulation, but were dissociated from the TLR4 signalosome by 30 min (Fig. 3 C and Fig. S3 H). However, the preassembled TLR4 complex with regulatory molecules, as well as the assembly of the Myddosome and Triffosome, were not observed in talin1-deficient DCs (Fig. 3 C), suggesting that the presence of talin1 in the preassembled TLR4 complex is required for the assembly of the TLR4 signalosome upon LPS ligation. Because the assembly of the Myddosome in talin1-deficient DCs upon LPS ligation was compromised, subsequent TLR4 down-regulation (Fig. 3 D), Triffosome assembly, and IRF3 activation (Fig. 3 B) were expectedly impaired. Interestingly, even though TLR4 signalosome assembly upon LPS stimulation was reduced in talin1-deficient BMDMs (Fig. S4 B), TLR4 down-regulation in these cells was less affected by talin1 deficiency (Fig. S4 C). Therefore, the observed preassembled TLR4 complex likely enables a rapid and efficient response to TLR stimulation in DCs compared with macrophages. Indeed, our data revealed more rapid down-regulation of TLR4 (Fig. 3 D and Fig. S4 C), as well as earlier and stronger activation of phospho-ERK (T202/Y204) and phospho-AKT (S473), in DCs than in macrophages (Fig. S4 D). In the absence

of preassembled complex, talin1 was recruited to TLR4 complex 30 min upon ligand binding in macrophages and dissociated from the complex 60 min after stimulation (Fig. S4 B). Collectively, talin1 is likely to be involved in TLR signaling pathways via similar mechanisms in DCs and macrophages. However, due to lack of preassembled TLR complex, macrophages respond less rapidly than DCs to TLR ligands.

Talin1 is required for the recruitment and activation of integrins in the preassembled TLR4 complex

Our data not only revealed that integrins (CD11b and CD29) were detectable in our TLR4 coimmunoprecipitation experiments (Fig. 3 C and Fig. S3 H), but also showed that TLR4 was present in talin1 and integrin coimmunoprecipitation studies (Fig. 4 A). Because membrane-localized talin1 usually binds to and activates integrins (Chinthalapudi et al., 2018; Ye et al., 2016), talin1 and integrins associated with membrane proximal TLR4/MyD88 complexes are likely to be functionally active. To determine whether the TLR4-associated integrin CD29 assumes an active configuration, we immunoprecipitated CD29 (integrin β1) and its associated proteins using an anti-CD29 antibody or an antibody against its active configuration (9EG7). Even though the anti-CD29 antibody pulled down much higher amounts of CD29 than the 9EG7 antibody, the associated TLR4 and downstream molecules were substantially enriched following IP with the 9EG7 antibody (Fig. 4 A), indicating that TLR4-associated integrins are mostly in the active configuration. Furthermore, the association of TLR4 with integrins or active integrins was strictly dependent on the presence of talin1 (Fig. 4 A). Concomitantly, LPS-stimulated talin1-deficient BMDCs (Fig. 4 B) or explant-cultured talin1-deficient LCs (Fig. 4 C) failed to effectively convert CD29 to its active configuration.

To determine whether the integrin binding and activating capacity of talin1 is crucial for its role in TLR4 signaling, we reconstituted talin1-deficient BMDCs with GFP-tagged talin1-W359A or talin1-L325R mutants, which either cannot bind integrins or can bind to but cannot activate integrins (Anthis et al., 2010; Wegener et al., 2007), respectively. We first validated the expressions of these talin1 mutants and verified their integrin-binding abilities (or lack thereof for talin1-W359A) by performing IPs for GFP-tagged talin1 followed by immunoblotting for GFP and the integrins CD11b and CD29 (Fig. 4 D). Furthermore, even though talin1-L325R was associated with integrins (Fig. 4 D), both talin1-L325R–bound integrins and integrins in talin1-W359A–expressing DCs were not activated upon binding to integrin ligand (Fig. 4 E). We also observed that while both talin1 mutants were able to interact with FAK (Fig. 4 D), the assembly of TLR4-associated regulatory molecules (CD11b, CD29, and talin1) and TLR4 signalosome proteins (MyD88, IRAK4, and TRIF) before and after stimulation were detected only in wild-type talin1 reconstituted talin1-deficient DCs (Fig. 4 F), suggesting that both the integrin-binding (W359) and -activating (L325) properties of talin1 are critical for TLR4 signaling in DCs. However, integrin outside-in signaling induced by ligand binding was not required for the preformed TLR4 complex and LPS-mediated pathways, because similar talin1-dependent complex formation and signalosome assembly were observed in control DCs under both adhesion (Fig. 3 C) and suspension culture conditions (Fig. 4 G).

Collectively, our data reveal that talin1 and active integrins are required for preassembly of the TLR4 complex with TIRAP/MyD88 and the recruitment of downstream signaling molecules upon TLR4-LPS ligation. Therefore, talin1 is likely to function as a scaffold protein that helps to assemble TLR4 signaling complexes under steady state and immediately upon LPS stimulation.

Talin1 regulates MyD88-dependent pathways in DCs via direct interaction with MyD88

Most of the currently identified TLRs share similar signaling pathways upon ligand engagement (Gay et al., 2014). To determine whether talin1 regulates signaling capacity downstream of other TLRs, we treated BMDCs with ligands for TLR1/2 (Pam3CSK4), TLR2/6 (MALP2), TLR5 (Flagellin), or TLR9 (CpG). Similar to LPS stimulation through TLR4, phosphorylation of AKT, phosphorylation and degradation of IκB, and up-regulation of CD86 and MHCII in talin1-deficient DCs were reduced following activation by these additional TLR ligands (Fig. 5, A–E), suggesting that talin1 regulates these TLR family members through a common mechanism. The less prominent reduction of CpG-induced IκB degradation in talin1-deficient DCs (Fig. 5 D) is likely due to the activation of other cytosolic DNA sensors (not depicted); hence the defective signaling capacity through TLR9 may be undervalued. Indeed, when we investigated the TLR9-associated complex in endosomes, the preassembled TLR9/MyD88 complex was abolished in talin1-deficient DCs (Fig. 5 F). Consequently, cytokine production upon MyD88-dependent ligand ligation was substantially reduced in talin1-deficient DCs (Fig. 5 G). Interestingly, the assembly of MyD88-independent TLR3 with TRIF-dependent complexes (Fig. 5 H) and activation of downstream TBK1/IRF3 upon poly(I:C) treatment were comparable in talin1-deficient and control DCs (Fig. 5 I). Notably, unlike other tested MyD88-dependent TLRs, talin1 was not associated with TLR3 (Fig. 5 H). IFNβ production upon poly(I:C) stimulation was not impaired by talin1 deficiency (Fig. 5 J). Thus, the defective assembly of TRIF-dependent complexes observed earlier in talin1-deficient DCs upon LPS stimulation is likely to be the consequence of a defective MyD88-dependent pathway, which is a prerequisite for TRIF-dependent events in the TLR4 signaling cascade. These data not only reveal that talin1 is dispensable for the assembly of the TLR3 signalosome, but also suggest that talin1 regulates the signaling capacity of MyD88-dependent TLRs in general.

It is feasible that talin1 controls MyD88-dependent TLR signaling pathways via direct interaction with MyD88. To test this possibility, we synthesized recombinant talin1 and MyD88 using a cell-free transcription/translation system and performed reciprocal IPs of talin1 and MyD88. Our results revealed a direct interaction between talin1 and MyD88 (Fig. 5 K). To identify the domains responsible for talin1–MyD88 interaction, we generated three Flag-tagged MyD88 fragments: the TIR-domain, the intermediate domain, and the death domain, as well as two GFP-tagged talin1 fragments for the head and rod domains. Full-length MyD88 or talin1, together with the respective truncated

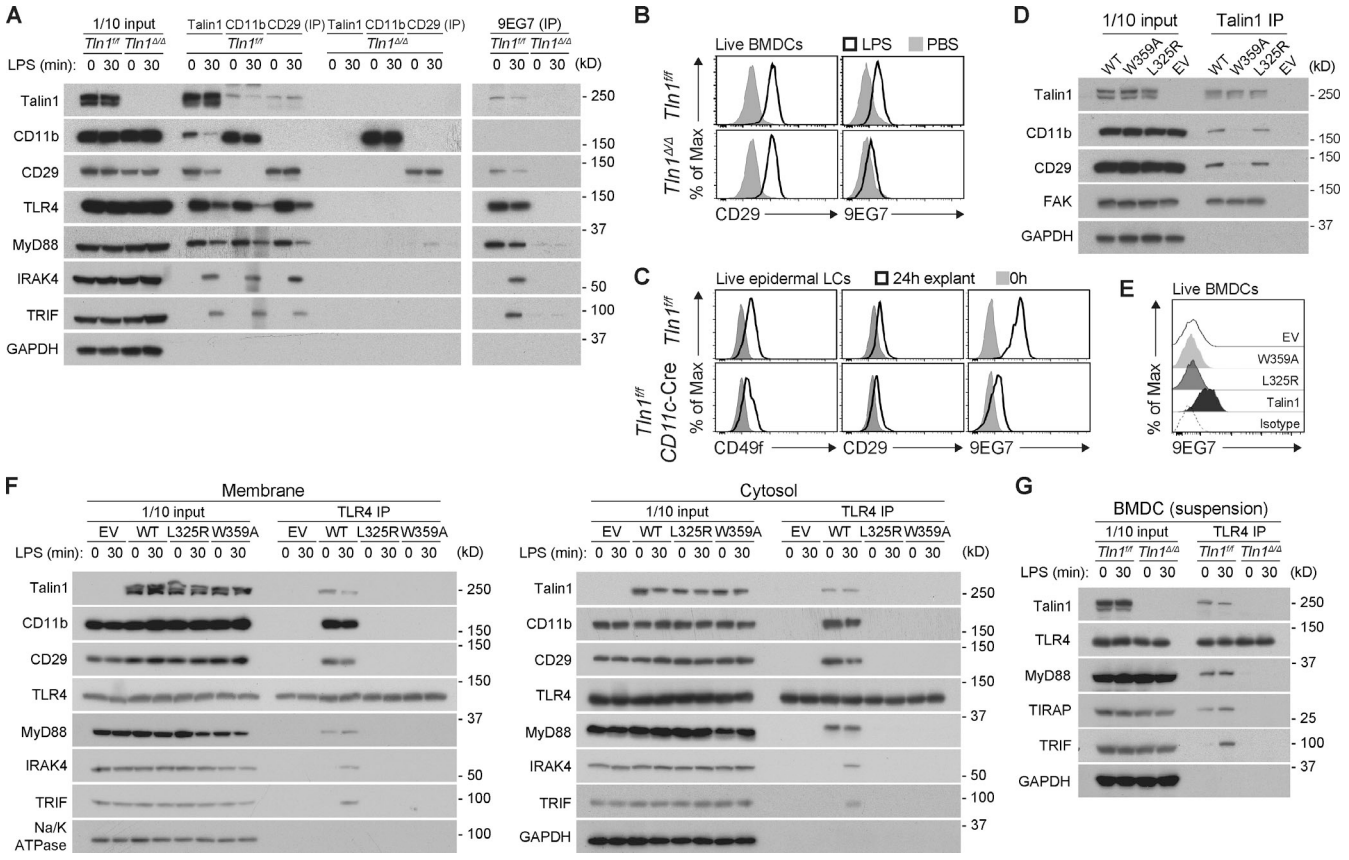

Figure 4. **Talin1 links integrins to TLR4 and contributes to DC activation. (A)** IPs of talin1, CD11b, CD29, and activated CD29 (9EG7) from total lysates of wild-type (*Tln1*$^{f/f}$) and talin1-deficient (*Tln1*$^{Δ/Δ}$) BMDCs stimulated with LPS (30 min), followed by immunoblot analysis. **(B and C)** Flow cytometric analysis of the indicated molecules on the surface of wild-type and talin1-deficient BMDCs stimulated with LPS overnight (B) or wild-type and talin1-deficient (*Tln1*$^{f/f}$*CD11c*-Cre) LCs isolated from 24-h explant cultures (C). Three independent experiments (n = 3 mice/group; C). **(D)** IP of GFP-tagged wild-type talin1, talin1-W359A, or talin1-L325R from total lysates of *Tln1*$^{Δ/Δ}$ BMDCs or *Tln1*$^{Δ/Δ}$ BMDCs reconstituted with wild-type talin1 or talin1 variants, followed by immunoblot analysis. **(E)** Histograms of active CD29 (9EG7) derived from flow cytometric analysis of *Tln1*$^{Δ/Δ}$ BMDCs and *Tln1*$^{Δ/Δ}$ BMDCs reconstituted with wild-type talin1 or talin1 variants and plated onto fibronectin-coated dishes for 30 min. **(F)** TLR4 IPs from membrane (left) and cytosol (right) fractions of LPS-stimulated talin1-deficient BMDCs (EV) or talin1-deficient BMDCs reconstituted with wild-type talin1 (WT) or talin1 variants (W359A or L325R), followed by immunoblot analysis. **(G)** TLR4 IPs from total lysates of wild-type and talin1-deficient BMDCs stimulated with LPS (30 min) in suspension, followed by immunoblot analysis. Inputs shown are as indicated in Fig. 3 C. GAPDH (total lysates or cytosolic fractions) and Na/K ATPase (membrane fractions) are shown as fractionation and loading controls (A, D, F, and G). Retroviral transduction of BMDCs was performed as described in Materials and methods. BMDCs were generated from the BM cells of poly(I)•poly(C)-treated *Tln1*$^{f/f}$ and *Tln1*$^{f/f}$*Mx*-Cre mice, as described in Fig. 1 F. Cells were pooled from two to three mice/group for each IP followed by immunoblot experiment. Data shown are representative or summaries of two (D and E) or three (A–C, F, and G) independent experiments.

fragments of their interaction counterparts, were transiently overexpressed in HEK-293T cells followed by IP using antibodies against Flag (MyD88) or GFP (Talin1). Using these reciprocal IPs, we identified and validated an interaction between the rod domain of talin1 and the intermediate domain of MyD88 (Fig. 5 L). We further confirmed the colocalization of talin1, MyD88, and TLR4 associated with MD2 (TLR4^{MD2}) by immunofluorescence staining (Fig. 5, M and N). Moreover, the colocalization of MyD88 and TLR4^{MD2} was significantly reduced in talin1-deficient DCs (Fig. 5 O). Based on these results, it is likely that the interaction between talin1 and MyD88 provides a scaffold for TLR4 complexes under steady state and within the first 10 min of stimulation. When talin1 is released from the preassembled TLR4 complex 30 min after stimulation, the intermediate domain of MyD88 becomes available for IRAK4 recruitment and the assembly of downstream signaling molecules (Burns et al., 2003; Lin et al., 2010).

Notably, the colocalization of talin1, MyD88, and TLR4^{MD2} was not detected in steady-state macrophages (Fig. S5, A and B), which was consistent with our earlier coimmunoprecipitation data (Fig. S4 B). Because DCs responded to LPS faster and more efficiently than macrophages (Fig. S4 D), we wondered, aside from the preassembled TLR4 complexes in DCs, if the density of TLR4 on the cell surface is different in DCs and macrophages. To test this, we determined the expression levels of surface TLR4^{MD2} and TLR4 on BMDCs and BMDMs by immunofluorescence staining. Our data revealed that surface TLR4 was mostly associated with MD2 in both cell types (Fig. S5, C and D). However, the lack of TLR4-MyD88 colocalization in BMDMs was even more apparent when only surface TLR4 or TLR4^{MD2} was taken into account (Fig. S5, C and D), compared with what was observed with staining for total TLR4^{MD2} (Fig. S5, A and B). In fact, the localization of TLR4 and MyD88 domains on the surface

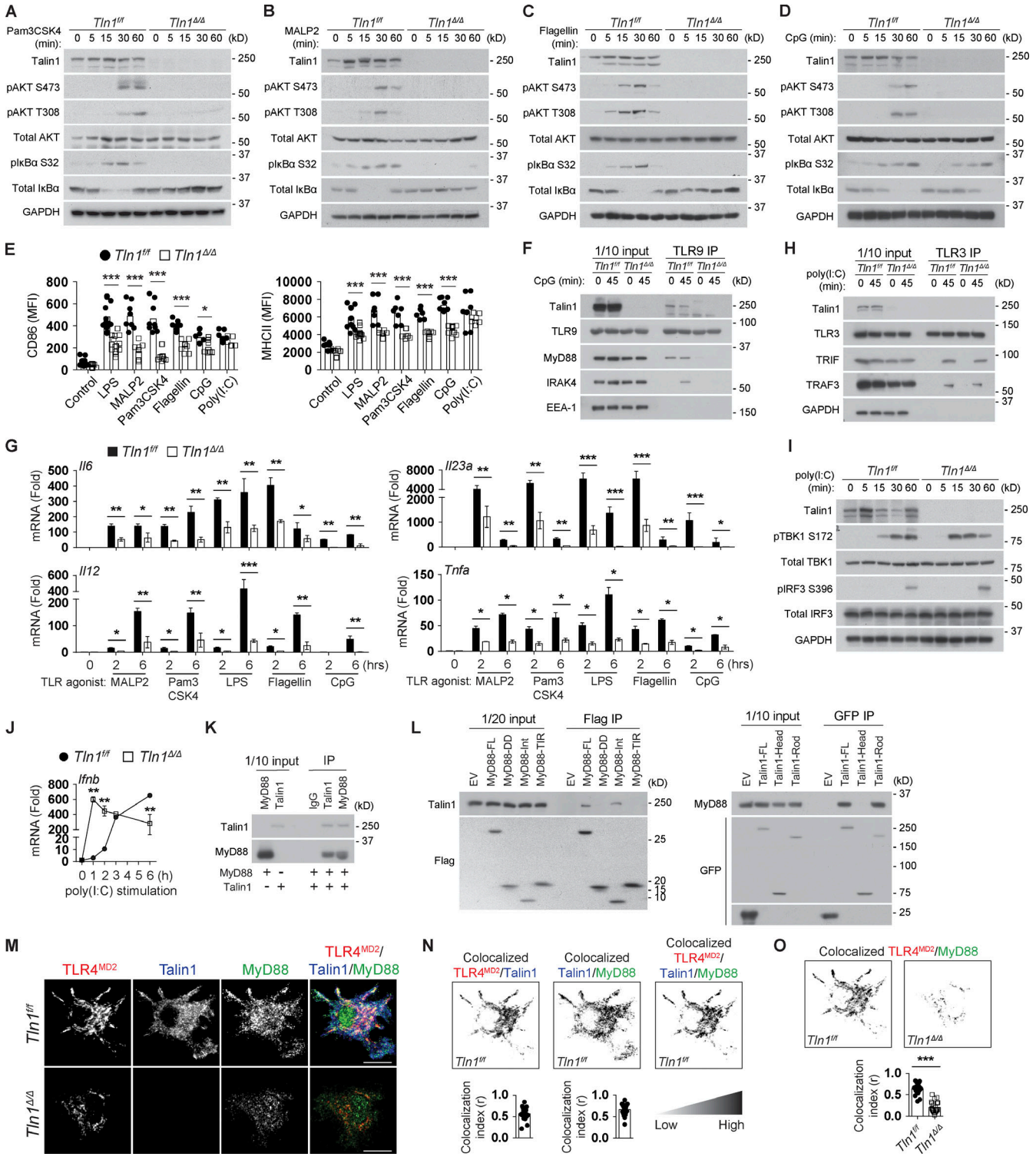

Figure 5. **Talin1 regulates MyD88-dependent TLR signaling pathways in DCs. (A–D)** Immunoblot analysis of control (*Tln1*$^{f/f}$) and talin1-deficient (*Tln1*$^{Δ/Δ}$) BMDCs stimulated with Pam3CSK4 (A), MALP2 (B), flagellin (C), or CpG (D) for the indicated times. **(E)** MFIs of CD86 (E, left) and MHCII (E, right) in matured control and talin1-deficient BMDCs upon TLR agonist stimulation, as determined by flow cytometric analyses. Data were pregated on singlet, live cells. BMDCs were defined as CD11c^{+}MHCII^{+}. Each data point in the scatter plots indicates the MFI of CD86 or MHCII in BMDCs. **(F)** TLR9 IP from purified endosomes of control (*Tln1*$^{f/f}$) and talin1-deficient (*Tln1*$^{Δ/Δ}$) BMDCs stimulated with CpG, followed by immunoblot analysis. **(G)** RT-qPCR results showing the mRNA expression levels of *Il6*, *Il12*, *Il23a*, and *Tnfa* in wild-type and talin1-deficient BMDCs stimulated with the indicated TLR agonists for 2 and 6 h. **(H)** TLR3 IP from total lysate of control (*Tln1*$^{f/f}$) and talin1-deficient (*Tln1*$^{Δ/Δ}$) BMDCs stimulated with poly(I:C), followed by immunoblot analysis. **(I)** Immunoblot analysis of control (*Tln1*$^{f/f}$) and talin1-deficient (*Tln1*$^{Δ/Δ}$) BMDCs stimulated with poly(I:C) for the indicated times. **(J)** RT-qPCR results showing the mRNA expression levels of *Ifnb1* in wild-type and talin1-deficient BMDCs stimulated with poly(I:C) for the indicated times. *Gapdh* was used as an internal control (G and J). **(K)** IP of recombinant talin1 and MyD88 synthesized in a cell-free expression system (see IVT assay). **(L)** IPs of full-length and truncated flag-tagged MyD88 (left, Flag IP) or GFP fusion

talin1 (right, GFP IP) fragments overexpressed in HEK-293T cells, followed by immunoblot analysis. 10% (1 of 10; F, H, K, and I) and 5% (1 of 20; I) of cell lysates used for IPs are shown as input controls. **(M)** Confocal image analysis of TLR4^{MD2} (red), MyD88 (green), and talin1 (blue) in wild-type and talin1-deficient BMDCs. Scale bars, 10 µm. **(N and O)** Colocalization analysis of TLR4^{MD2}/Talin1, Talin1/MyD88, and TLR4^{MD2}/Talin1/MyD88 in control (*Tln1*$^{f/f}$) BMDCs (n = 20 cells; N) and TLR4^{MD2}/MyD88 in control (*Tln1*$^{f/f}$) and talin1-deficient (*Tln1*$^{\Delta/\Delta}$) BMDCs (n = 20 cells/group; O). Representative images (top) and Spearman's correlation coefficients, r (bottom) are shown. Image intensities correspond to the degree of colocalization between the indicated molecules. Each point in the scatter bar graphs indicates the Spearman's correlation coefficient from one cell. 20 cells pooled from three experiments were scored. The ImageJ plugin Coloc 2 was used for the colocalization analysis of the images shown. The AND operator of the Image Calculator (ImageJ) was used to overlay the images. See Materials and methods for further details. BMDCs were generated from the BM cells of poly(I)•poly(C)-treated *Tln1*$^{f/f}$ and *Tln1*$^{f/f}$*Mx*-Cre mice, as described in Fig. 1 F. Cells were pooled from two to three mice/group for each IP followed by immunoblot experiment. Data shown are representative or summaries of two (A, B, and D) or three (C and E–O) independent experiments. E, n = 7 mice; G and J, mean ± SD. *, 0.01 < P ≤ 0.05; **, 0.005 < P ≤ 0.01; and ***, P ≤ 0.005 (two-tailed Student's t test, unless stated otherwise).

of BMDMs was mutually exclusive (Fig. S5, C and D). Collectively, our data suggest that a high level of surface TLR4^{MD2}/TIRAP/MyD88 is likely to license DCs to respond rapidly and efficiently to ligand engagement.

Talin1 promotes PIP2-mediated recruitment of TIRAP to TLR4 in DCs

Although direct interaction of talin1 with MyD88 explains the presence of talin1 in the TLR complex, it is unclear how the recruitment of TIRAP is negatively affected by talin1 deficiency. Because talin is reported to associate with and activate PIP5K in fibroblasts, and PIP5K catalyses the production of PIP2 (Di Paolo et al., 2002; Ling et al., 2002), which could help recruit TIRAP to the plasma membrane (Kagan and Medzhitov, 2006), we decided to investigate the association between PIP5K and talin1 in relation to TLR4 in DCs. We found that PIP5K coprecipitated with TLR4, talin1, and active integrin in control, but not talin1-deficient, DCs (Fig. 6 A). Furthermore, siRNA-mediated PIP5K knockdown in BMDCs demonstrated that PIP5K was essential for the recruitment of TIRAP, MyD88, and talin1 to the preassembled TLR4 complex in steady-state and downstream signaling pathways upon LPS stimulation (Fig. 6 B). The colocalization of PIP2, TIRAP, and TLR4^{MD2} was also analyzed by immunofluorescence staining in DCs prepared using cytospin. We found that this protocol preserved PIP2 clusters better than staining cells adherent to the culture plate. Our data revealed that TIRAP/TLR4^{MD2} clusters were large and abundant and were frequently associated with PIP2 in control, but not talin1-deficient, DCs (Fig. 6 C). The size and number of TIRAP/PIP2 clusters in control and talin1-deficient DCs was further analyzed by ImageJ (National Institutes of Health) using binary images (Fig. 6 D, left). Significantly smaller TIRAP/PIP2 clusters in reduced quantities were detected in talin1-deficient DCs compared with control cells (Fig. 6 D, right). However, the overall amount of PIP2, as measured by flow cytometric analysis, was comparable in talin1-deficient and control DCs (Fig. 6 E). PIP2 can also be converted by phospholipase C to produce two well-characterized second messengers: diacylglycerol and inositol 1,4,5-triphosphate (IP3; Prole and Taylor, 2019). IP3 is involved in the release of Ca^{2+} from the endoplasmic reticulum to increase the concentration of intracellular Ca^{2+} (Berridge, 1993; Prole and Taylor, 2019), so we decided to see whether there were any changes in Ca^{2+} flux in the absence of talin1. Indeed, reduced Ca^{2+} flux was observed in talin1-deficient DCs treated with LPS (Fig. 6 F, top), compared with control cells, which could be due to the reduced numbers of TLR4^{MD2}/PIP2 clusters in cells lacking talin1. Similar reductions in Ca^{2+} flux were also detected in talin1-deficient DCs upon TLR1/2 (Pam3CSK4) stimulation (Fig. 6 F bottom left). However, comparable levels of ionophore-induced Ca^{2+} flux were observed in DCs with or without talin1 (Fig. 6 F, bottom right), demonstrating that the Ca^{2+} signaling capacity of talin1-deficient DCs was intact. PIP2 also functions as a substrate for PI3-kinase to generate PI 3,4,5-trisphosphate, which recruits and activates PH domain–containing molecules such as AKT. The reduced AKT activation in LPS-stimulated talin1-deficient DCs, as shown earlier (Fig. 3 B), could also be caused by the low number of TLR4^{MD2}/TIRAP/PIP2 clusters observed in the absence of talin1. Collectively, our data suggest that talin1 controls TLR signaling complexes under steady state by bringing PIP5K/active integrin into the proximity of TLRs, thus creating favorable conditions for TLR complex preassembly.

Talin1 controls DC-mediated antibacterial immune responses

Having identified the novel regulatory mechanism for talin1 in DC activation, we sought to determine its physiological relevance in vivo. To address this question, we chose a mouse model of cutaneous bacterial infection, not just because *Staphylococcus aureus* is a commensal and a common skin and systemic pathogen, but also because there are strains of methicillin-resistant *S. aureus* (MRSA), such as USA300, causing widespread nosocomial infections (Tong et al., 2015). Hence, we used this clinically relevant *S. aureus* USA300 strain to study the role of talin1 in DC activation in vivo. MRSA is a Gram-positive pathogen whose cell wall products, such as peptidoglycans, lipoteichoic acid, and lipoproteins, trigger the activation of DCs via the TLR2 signaling cascade (Gay et al., 2014; Kawasaki and Kawai, 2014; Thammavongsa et al., 2015), which was previously shown to be regulated by talin1 (Fig. 5, A and B). Here, control and *Tln1*$^{f/f}$-*CD11c*-Cre mice were epicutaneously infected with *S. aureus* USA300, and cytokine expression profiles of T cells from the sdLNs were examined 6 d after infection. We found that the numbers of IFNγ–producing CD4$^+$ and CD8$^+$ T cells, TNFα-producing CD4$^+$ and CD8$^+$ T cells, IL-17–producing CD4$^+$ T cells, and the less-studied IL-17–producing CD8$^+$ T cells were significantly reduced in mice with talin1-deficient DCs (Fig. 7 A). These results correlate well with the reduced numbers of talin1-deficient migratory DCs (mDCs) in the sdLNs (Fig. 7 B) with lowered levels of surface MHCII expression (Fig. 7 C). Accordingly, defective AKT and NFκB activation were observed in talin1-deficient BMDCs treated with heat-killed *S. aureus* in vitro

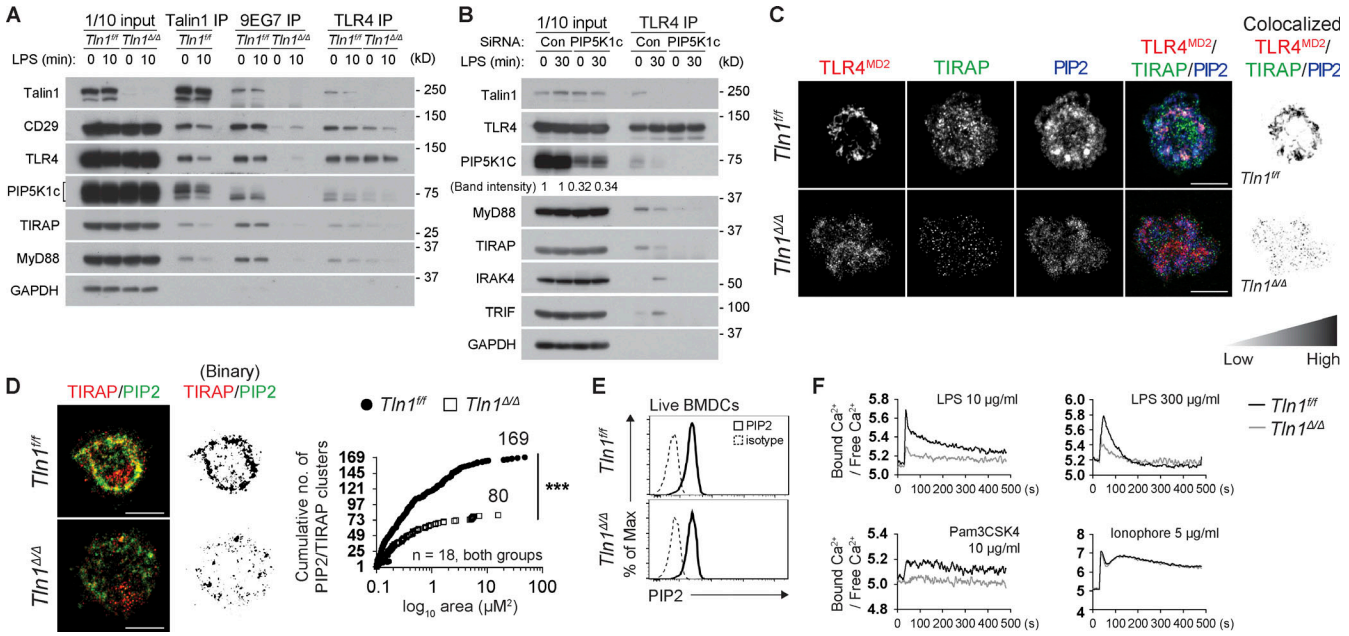

Figure 6. **PIP5K controls the assembly of preformed TLR4 complexes in DCs. (A)** IP of talin1, activated CD29 (9EG7), and TLR4 from total cell lysates of control (*Tln1*$^{f/f}$) and talin1-deficient (*Tln1*$^{Δ/Δ}$) BMDCs stimulated with LPS, followed by immunoblot analysis. **(B)** TLR4 IP of control (Con) or PIP5K1c siRNA-transfected wild-type BMDCs stimulated with LPS, followed by immunoblot analysis. 10% (1 of 10) of cell lysates used for IPs were run as input controls (A and B). **(C)** Confocal analysis of TLR4^{MD2} (red), TIRAP (green), and PIP2 (blue), as well as the colocalization of TLR4^{MD2}/TIRAP/PIP2 (right) in wild-type and talin1-deficient BMDCs. Image intensity corresponds to the degree of colocalization of the indicated molecules. The AND function of the Image Calculator (ImageJ) was used to overlay the images. Scale bars, 10 µm. **(D)** To better quantify the colocalized TIRAP/PIP2 clusters in merged immunofluorescence images (left, yellow), binary black-and-white images were generated (right) using the ImageJ binary filter. The number of TIRAP/PIP2 clusters and area of each cluster in control (total 169 clusters, *n* = 18 cells) and talin1-deficient BMDCs (total 80 clusters, *n* = 18 cells) are shown in the cumulative graph (right). Each point represents an individual cluster in a cell. Cumulative number of clusters on the y axis indicates the cumulative number of TIRAP/PIP2 clusters. Significance was determined using the Wilcoxon signed-rank test. Scale bars, 10 µm. See Materials and methods for further details. **(E)** Flow cytometric analysis of PIP2 in control and talin1-deficient BMDCs. **(F)** Ratiometric analysis of calcium flux as determined by [bound Ca^{2+}/free Ca^{2+}] in Indo-1 AM–loaded control and talin1-deficient BMDCs stimulated with LPS or ionophore as a positive control. Each point represents the ratio of [bound Ca^{2+}/free Ca^{2+}] at a specific time point. BMDCs were generated from the BM cells of poly(I)•poly(C)-treated *Tln1*$^{f/f}$ and *Tln1*$^{f/f}$*Mx*-Cre mice, as described in Fig. 1 F. Cells were pooled from two to three mice/group for each IP followed by immunoblot experiment. Data shown are summaries (D, right) or representative of three independent experiments. ***, P ≤ 0.005 (two-tailed Student's *t* test, unless stated otherwise).

(Fig. 7 D). The compromised DC response in *Tln1*$^{f/f}$*CD11c*-Cre mice was also correlated with the decreased number of infiltrating leukocytes and skin thickness on day 8 (Fig. 7, E and F), as well as increased *S. aureus* load on days 6, 9, and 12 (Fig. 7 G). Because various mDC subsets have been demonstrated to be potent inducers of Tc, Th1, and Th17 responses in other cutaneous infection models (Kashem et al., 2015), it is likely that both activation and migratory defects of talin1-deficient LCs and dDCs contribute to the compromised differentiation/polarization of various effector T cells upon MRSA infection.

Talin1 expression in DCs regulates skin tolerance toward innocuous hapten

To further explore the relevance of talin1-regulated DC activation under noninfectious conditions with defined roles for each cutaneous DC subset, we decided to investigate the small-molecule hapten-induced immune response. Contact hypersensitivity (CHS) induced by contact sensitizers, such as the strong hapten 2,4-dinitrofluorobenzene (DNFB), is a mouse model for the human disease allergic contact dermatitis, which is associated with cytotoxic T cell–mediated skin inflammation. In this model, the effector T cell response is largely regulated by skin DCs (Clausen and Stoitzner, 2015; Kaplan, 2017). To determine whether compromised activation and migration of talin1-deficient DCs affects CHS, we sensitized both control and *Tln1*$^{f/f}$*CD11c*-Cre mice with DNFB (0.5%), followed by ear challenge 5 d later with DNFB (0.1%) to induce CHS. In these experiments, we observed no significant difference in the magnitude of ear swelling (Fig. 8 A, top); however, an increased number of wild-type ($CD103^+CD11b^-$ and $CD103^-CD11b^+$) and talin1-deficient ($CD103^-CD11b^+$) mdDCs on day 2 as well as wild-type LCs on day 3 was detected in the sdLNs of 0.5% DNFB-sensitized mice compared with vehicle-painted littermates (Fig. 8 B). Even though the number of all talin1-deficient skin DC subsets was lower than what was observed for their wild-type counterparts in the sdLNs (Fig. 8 B), the amount was still sufficient to mount a substantial immunogenic response (ear swelling; Fig. 8 A, top). Consistent with the ear swelling results, the number of IFNγ-producing $CD8^+$ cytotoxic T cells in control mice and mice with talin1-deficient DCs was comparable (Fig. 8 C). These data revealed that skin DCs lacking talin1 are able to induce skin inflammatory responses, which is rather unexpected. It is possible that the dosage of DNFB (0.5%) was too high, sufficiently triggering talin1-deficient skin DCs to present

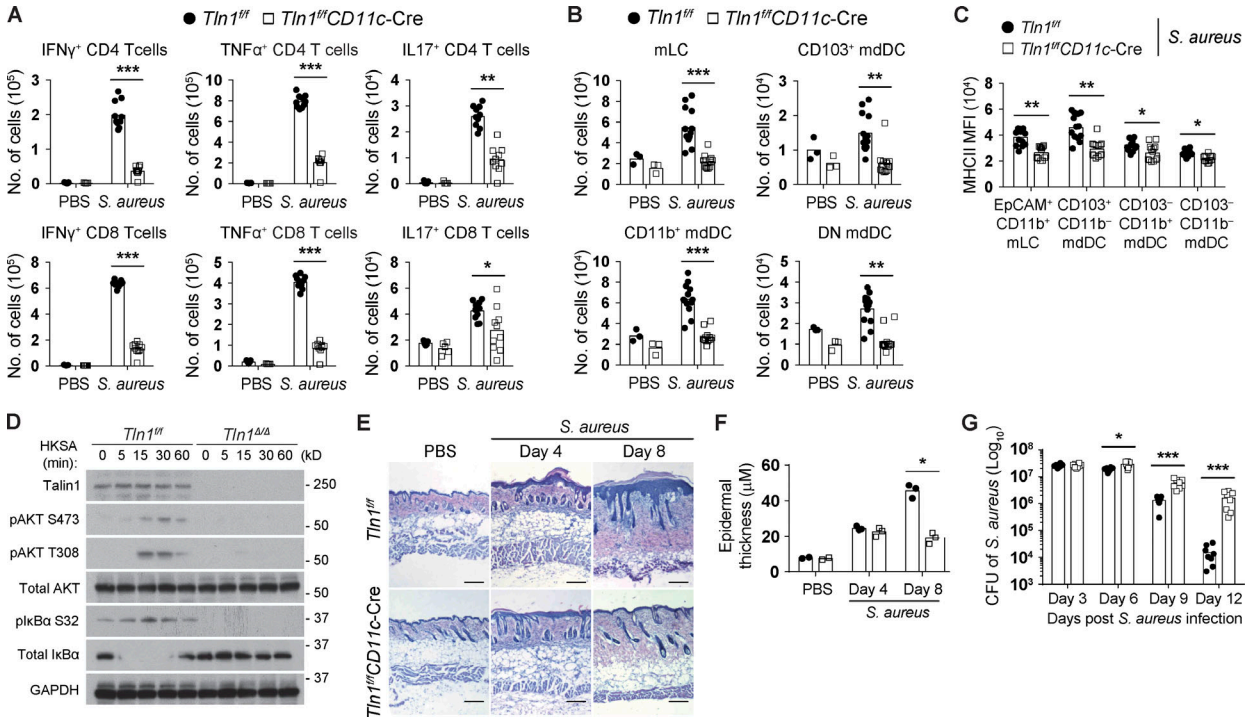

Figure 7. **Compromised immunity against *S. aureus* in mice with talin1-deficient DCs. (A)** Absolute numbers (scatter plots) of IFNγ-producing, TNFα-producing, and IL-17–producing CD4$^+$ or CD8$^+$ T cells in the sdLNs of control (*Tln1*$^{f/f}$) and *Tln1*$^{f/f}$*CD11c*-Cre mice 6 d after epicutaneous *S. aureus* infection. T cells were restimulated with PBDu and ionophore with brefeldin A for 5 h. **(B and C)** Absolute numbers (scatter plots; B) and MHCII expression (MFI; C) of mDC subsets in sdLNs 3 d after epicutaneous *S. aureus* infection. Each data point represents an individual mouse (A–C). Three independent experiments; *n* = 3 mice/group (PBS) or *n* = 10–12 mice/group (*S. aureus*; A–C). **(D)** Immunoblot analysis of control and talin1-deficient BMDCs stimulated with heat-killed *S. aureus* (HKSA) for the indicated times. BMDCs were generated from the BM cells of poly(I)•poly(C)-treated *Tln1*$^{f/f}$ and *Tln1*$^{f/f}$*Mx*-Cre mice, as described in Fig. 1 F. **(E and F)** H&E–stained skin sections (E) and skin epidermal thickness (F) of control (*Tln1*$^{f/f}$) and *Tln1*$^{f/f}$*CD11c*-Cre mice 4 and 8 d after epicutaneous *S. aureus* infection. Each data point represents an individual mouse (F). Two independent experiments; *n* = 2 mice/group (PBS) or *n* = 3 mice/group (*S. aureus*). **(G)** CFUs of *S. aureus* in skin lesions of control and *Tln1*$^{f/f}$*CD11c*-Cre mice 3, 6, 9, and 12 d after initial infection. Three independent experiments (*n* = 6–8 mice/group per condition). Data shown are representative or summaries of two (E and F; mean ± SD) or three (A–D and G; mean ± SD) independent experiments. *, 0.01 < P ≤ 0.05; **, 0.005 < P ≤ 0.01; ***, P ≤ 0.005 (two-tailed Student's *t* test).

enough antigen to naive T cells in sdLNs compensating for any migratory or functional defects of talin1-deficient skin DCs. Hence, we next treated both control and *Tln1*$^{f/f}$*CD11c*-Cre mice with a low dose of DNFB (0.008%), according to the concept established by Noordegraaf et al. (2010). Interestingly, significant ear swelling was detected in control mice, but not in *Tln1*$^{f/f}$*CD11c*-Cre mice (Fig. 8 A, bottom), which corresponded with increased numbers of IFNγ-producing CD8$^+$ cytotoxic T cells (Fig. 8 C) and wild-type CD103$^-$CD11b$^+$ mdDCs (Fig. 8 B) in sdLNs. In contrast, the number of IFNγ-producing CD8$^+$ cytotoxic T cells (Fig. 8 C) and talin1-deficient skin DC subsets (Fig. 8 B) in the sdLNs of *Tln1*$^{f/f}$*CD11c*-Cre mice painted with low-dose DNFB remained comparable to vehicle-painted (unsensitized) *Tln1*$^{f/f}$*CD11c*-Cre mice. These findings are in line with previous reports (Kel et al., 2010; Noordegraaf et al., 2010), suggesting that talin1 expression in skin DCs, in particular LCs and CD103$^-$CD11b$^+$ dDCs, is required for low-dose hapten-induced CHS response. Moreover, talin1-deficient CD103$^-$CD11b$^+$ mdDCs are likely to compensate for the suboptimal DC activation and migration during CHS response induced by high-dose hapten in *Tln*$^{f/f}$*CD11c*-cre mice.

The tolerogenic properties of LCs and their ability to protect against cutaneous allergy and autoimmune disease have been well documented (Gomez de Agüero et al., 2012; King et al., 2015). Because LC migration out of the skin is essential for controlling allergic skin inflammation (Kaplan, 2017; Loh et al., 2018), and talin1-deficient LCs display reduced trafficking to sdLNs (Fig. 1, A–E), the tolerance induction in mice with talin1-deficient DCs is likely to be defective. Here, control and *Tln1*$^{f/f}$*CD11c*-Cre mice were tolerized with the weak hapten DNTB, followed by CHS induction (sensitized with 0.5% DNFB and challenged with 0.1% DNFB; Fig. 8 D). Because the innocuous DNTB generates dinitrophenyl–self peptide motifs similar to those of the strong hapten DNFB, T cell antigen–specific tolerization can be induced using this approach (Gomez de Agüero et al., 2012). Here, we observed that tolerization with DNTB was able to suppress the development of DNFB-induced ear swelling in control mice (Fig. 8 D). In contrast, *Tln1*$^{f/f}$*CD11c*-Cre mice developed a robust CHS response that peaked at day 2–3 despite prior DNTB treatment, implying compromised induction of cutaneous tolerance (Fig. 8 D). Accordingly, sdLNs from these animals contained reduced numbers of activated regulatory T cells (T reg cells; ICOS$^+$Foxp3$^+$; Fig. 8 E) and increased numbers of IFNγ-producing CD8$^+$ T cells (Fig. 8 F). As expected, although control LCs efficiently migrated away from the DNTB-painted

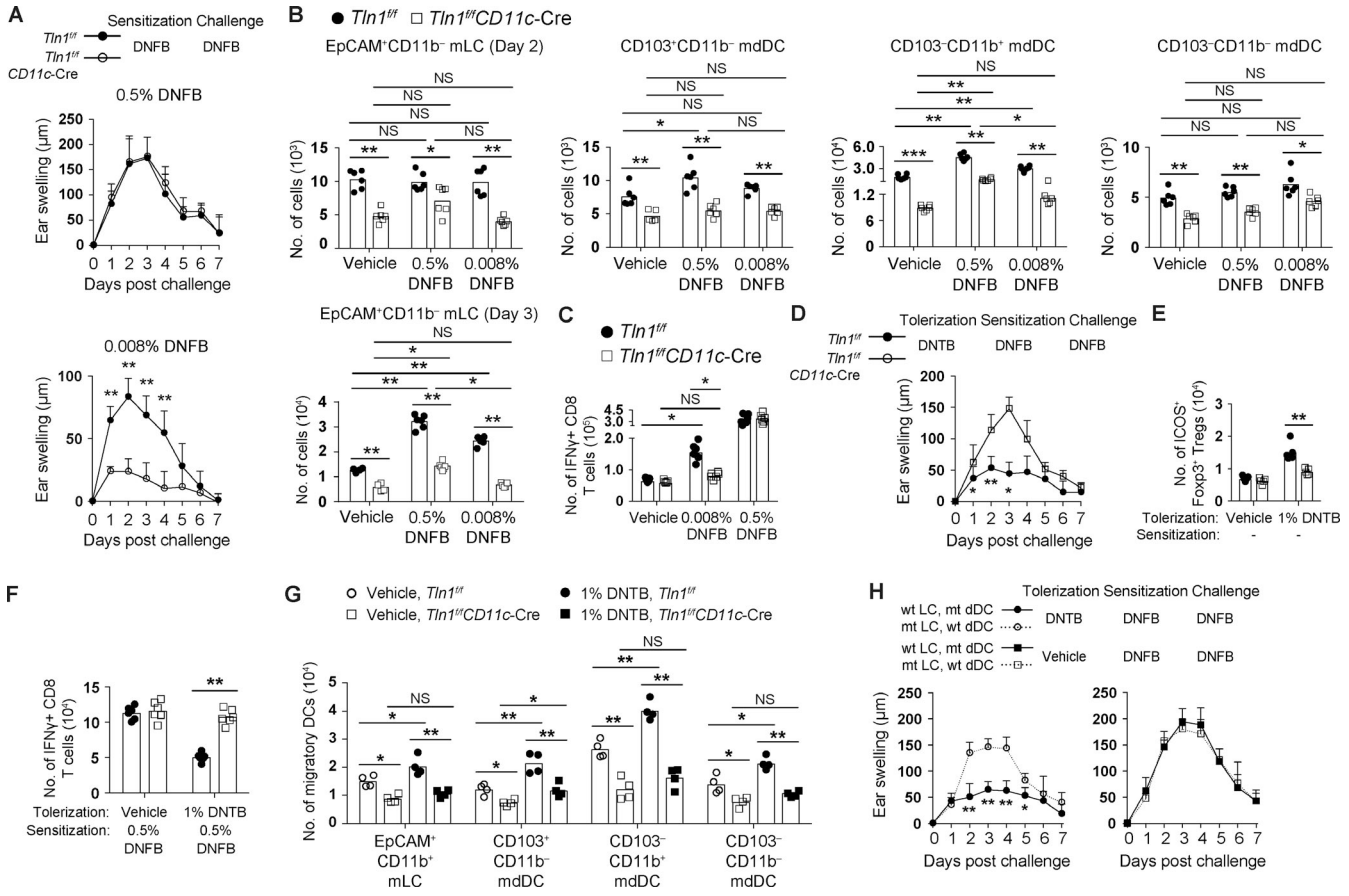

Figure 8. **Talin1 expression in skin DCs controls immune responses against hapten. (A)** Ear swelling responses (bottom) of mice sensitized with 0.5% or 0.008% DNFB, followed by ear challenge 5 d later with 0.1% DNFB (top, experimental outline). Five independent experiments (n = 8 mice/group). **(B)** Absolute numbers (scatter plots) of DC subsets in the sdLNs of *Tln1*$^{f/f}$ and *Tln1*$^{f/f}$*CD11c*-Cre mice sensitized with 0.5% or 0.008% DNFB 2 d after DNFB painting unless stated otherwise. Vehicle (acetone:olive oil) was used as control. Three independent experiments (n = 6 mice/group per condition). Day 3 data are derived from 4–6 mice. **(C)** Absolute numbers (scatter plots) of IFNγ-producing CD8$^+$ T cells in the sdLNs of *Tln1*$^{f/f}$ and *Tln1*$^{f/f}$*CD11c*-Cre mice sensitized with 0.5% or 0.008% DNFB 5 d after DNFB painting. Four independent experiments (n = 6 mice/group per condition). **(D)** Ear swelling responses (bottom) of DNTB-tolerized, DNFB-sensitized and challenged mice over a period of 7 d. Mice were tolerized with 1% DNTB on shaved abdomen skin. 7 d later, mice were sensitized with 0.5% DNFB on shaved back skin and ear challenged 5 d later with 0.1% DNFB (top, experimental outline). Five independent experiments (n = 8 mice/group). **(E)** Absolute numbers (scatter plots) of ICOS$^+$CD4$^+$Foxp3$^+$ T reg cells in the sdLNs of *Tln1*$^{f/f}$ and *Tln1*$^{f/f}$*CD11c*-Cre mice 5 d after vehicle painting or DNTB tolerization. Data were pregated on singlet, live CD3$^+$CD4$^+$Foxp3$^+$ T reg cells. Five independent experiments (n = 5 mice/group). **(F)**, Absolute numbers (scatter plots) of IFNγ-producing CD8$^+$ T cells in the sdLNs of *Tln1*$^{f/f}$ and *Tln1*$^{f/f}$*CD11c*-Cre mice tolerized with 1% DNTB and sensitized with 0.5% DNFB. Inguinal LNs were harvested 5 d after DNFB sensitization. Five independent experiments (n = 5 mice/group). T cells were restimulated with PBDu and ionophore with brefeldin A for 5 h (C and F). **(G)** Absolute numbers (scatter plots) of DC subsets in sdLNs 3 d after 1% DNTB painting on shaved mouse trunk skin. Vehicle was used as control. Three independent experiments (n = 4–6 mice/group). **(H)** Chimeric mice, generated as described in Materials and methods, were tolerized with 1% DNTB, sensitized, and challenged with DNFB as described in D (top, experimental outline). Ear swelling of DNTB-tolerized, DNFB-sensitized and challenged BM chimeric mice over a period of 7 d. Three independent experiments (n = 4–6 mice/group). Data were pregated on singlet, live cells (B, C, and E–G). Each data point represents an individual mouse (B, C, and E–G). Data shown are representative or summaries of five (A and D, mean ± SEM; E and F, mean ± SD), four (C and E; mean ± SD) or three (B and G, mean ± SD; H, mean ± SEM) independent experiments. *, 0.01 < P ≤ 0.05; **, 0.005 < P ≤ 0.01; ***, P ≤ 0.005 (two-tailed Student's t test).

epidermis, talin1-deficient LCs were unable to exit the skin when exposed to the same treatment (Fig. 8 G).

Because DNTB induced the migration of control dDCs to sdLNs in significantly higher numbers than talin1-deficient dDCs (Fig. 8 G), we sought to verify that talin1-deficient LCs are indeed responsible for the defective tolerance induction. Taking advantage of the radioresistant feature of LCs, we performed a series of BM transplant experiments to selectively delete talin1 in either LCs or dDCs. Using the same tolerization and sensitization regimen employed in our previous experiments, we observed increased ear swelling in BM chimeric mice lacking talin1 only in epidermal LCs (Fig. 8 H, left). In contrast, ear inflammation was significantly reduced in BM chimeras whose skin was populated by wild-type LCs and talin1-deficient dermal DCs (Fig. 8 H, left). Importantly, when both groups of chimeric mice were painted with two consecutive doses of DNFB to induce CHS without prior tolerization, we observed no significant difference in the magnitude of ear swelling (Fig. 8 H, right). These results are consistent with the findings of earlier reports (Gomez de Agüero et al., 2012; Loh et al., 2018) and confirm the critical role of mLCs in promoting skin tolerance via T reg cell activation in sdLNs. Moreover, our data indicate that

talin1-regulated LC migration to sdLNs critically contributes to the induction of tolerance against skin cutaneous allergens.

Discussion

Here, we report that talin1 association with TLRs via direct interactions with MyD88 and PIP5K promotes the formation of preassembled TLR complexes that are required for downstream signaling events upon ligand engagement in DCs. Our studies demonstrate that talin1/integrin not only is involved in cell adhesion and migration, but also critically regulates the maturation and activation of DCs.

By dissecting the roles of the different DC subpopulations in the skin, we identified impaired integrin-dependent transmigration of talin1-deficient LCs across the basement membrane. However, the reduced numbers of mLCs in the dermis and sdLNs were due not only to defective integrin activation. In fact, the activation and maturation of talin1-deficient LCs and other skin DCs were compromised in the presence of LPS or other TLR ligands. E-cadherin down-regulation on LCs and MHCII or CD86 up-regulation on all skin DCs, as well as BMDCs, were impaired in the absence of talin1. Even though talin1-deficient LCs up-regulated the expression of metalloproteinases MMP2/9, which may enable a limited number of cells to traverse the basement membrane by increasing the porosity of the substratum (Ratzinger et al., 2002), the number of migrating LCs was still not sufficient to rescue the physiological functions of LCs in our in vivo mouse models. In addition, the talin1 isoform talin2, as well as the integrin coactivator kindlin3, were not up-regulated to compensate for the loss of talin1 in LCs. Consequently, LC-dependent immune responses, such as Th17 induction in microbial infection and tolerance induction against innocuous hapten, were impaired.

Interestingly, up-regulation of CCR7 was not affected by talin1 deficiency. *Ccr7* expression can potentially be transcriptionally regulated by Foxo1 (Dong et al., 2015), AP-1, and NFκB (Bovay et al., 2018), whereas IFNβ secreted by LPS-stimulated DCs is shown to negatively regulate *Ccr7* expression. Because we observed reduced NFκB activation and IFNβ production by talin1-deficient LCs and BMDCs, it is possible that the positive and negative influences caused by talin deficiency equilibrates, and the final CCR7 expression on control and talin1-deficient cells becomes comparable.

Defective talin1-deficient dDC and BMDC migration in vivo and in vitro is rather unexpected, since a previous report showed that talin1 deficiency does not affect the 3D migratory capacity (Lämmermann et al., 2008) of DCs. In these studies, when control and talin1-deficient BMDCs were injected i.d. into footpads, comparable numbers of cells were recovered from sdLNs (Lämmermann et al., 2008). In this experimental setting, the number of injected BMDCs far exceeds the number of endogenous skin DCs; therefore, the collective migration, as a result of high cell density (Park and Doh, 2019) or inflammation caused by the injection, may have compensated for the compromised activation and migration of talin1-deficient BMDCs. In contrast, the migratory defect of talin1-deficient DCs demonstrated in our study was derived from endogenous dDCs under steady state or physiologically relevant inflammatory conditions. We also observed a significant reduction in chemokine-induced 3D migration of talin1-deficient BMDCs, in contrast to the previous study. Notably, the migration speed of control cells exposed to the same concentration of chemokine is higher in our study than that observed in the earlier study (Lämmermann et al., 2008), whereas the migration speed of talin1-deficient DCs is comparable in both studies. It is probable that our culture conditions may have permitted optimal migration of control DCs, hence revealing migratory differences in control and talin1-deficient DCs.

The presented novel talin1-mediated regulation mechanism of the TLR signaling pathway appears to be unique to DCs, since macrophages do not form preassembled TLR/MyD88 complexes under steady state, and the down-regulation of TLR4 upon LPS stimulation is not affected by CD11b (Ling et al., 2014) or talin1 deficiency. In both cell types, regardless of preassembled TLR complexes, Myddosome assembly upon TLR4-LPS ligation was impaired or reduced in the absence of talin1. So, why do DCs form preassembled TLR/MyD88 complexes containing talin1? Aside from activation and pathogen phagocytosis, DCs also undergo rapid morphological and molecular changes (Faure-André et al., 2008; Vargas et al., 2016) to become mature DCs with enhanced migratory capacities. Thus, preassembled TLR complexes in DCs may allow them to quickly initiate activation and maturation. Indeed, our data demonstrate that DCs respond faster and more robustly to TLR ligand stimulation than macrophages.

The role of integrins in the activation of innate leukocytes, thus far, has been controversial. IRF3 and p65 activation are enhanced and prolonged in CD11b-deficient (*Itgam*$^{-/-}$) macrophages because of compromised Cbl-b–mediated degradation of MyD88 and TRIF (Han et al., 2010). In addition, CD11b has been shown to negatively regulate TLR9 activation in DCs through the up-regulation of miR-146a (Bai et al., 2012). However, Botto and colleagues (Ling et al., 2014) demonstrated in 2014 that CD11b positively regulates TLR4-induced signaling pathways in DCs, but not in macrophages. CD11b appears to regulate TLR-mediated cell activation through various mechanisms in different cell types. Moreover, deletion of a single integrin subunit in innate leukocytes may be compensated for by other integrins, which is fundamentally different than talin1 knockout cells, in which all integrin-mediated functions are abolished. Our data revealed that TLR4 associates either with CD11b (integrin αM, usually dimerizes with CD18 [integrin β2]) or CD29 (integrin β1), but not both at the same time (Fig. 4 A). It would be interesting to determine if TLRs associated with CD11b/CD18 or CD29 exhibit different signaling capacities.

Integrins could also contribute to DC activation through extracellular matrix engagement or cell–cell interactions, similar to what has been reported for T cells (Zhang and Wang, 2012). However, our data showed that the preassembly of TLR4 complexes and the formation of TLR4-mediated signalosome in control DCs under adhesion and suspension conditions were comparable. Furthermore, defective TLR4-mediated DC activation in talin1-deficient DCs was observed under both adhesion and suspension culture conditions. Taken together, our results

indicate that both the integrin binding and activation capacities of talin1 (inside-out activation of integrins) are important for TLR4 complex preassembly and LPS-induced TLR4 signal transduction; however, the external ligand binding of integrins (outside-in signaling component) is unlikely to be critical for DC activation. In fact, extracellular domain of integrin is reported to work with LPS binding protein and CD14 to promote LPS binding to TLR4/MD2 complexes (Wong et al., 2007).

Our results also provide a mechanistic explanation for the cross talk between TLRs and the PI3K/AKT pathway, which has been reported in various cell types under different physiological contexts (Manning and Toker, 2017). Activation of PI3K/AKT signaling is thought to limit proinflammatory and apoptotic events induced by the TLR/NFκB pathway. However, the molecular mechanism linking these pathways is not well understood. Here, aside from the TLR-associated regulatory subunit of PI3K, p85, our data further suggest that PIP5K can be recruited to TLR through interaction with talin1, thereby increasing the local concentration of PIP2. Elevated PIP2 levels not only enhance the recruitment of TIRAP, but also serve as a substrate for PI3K to synthesize PIP3, which is required for the recruitment and activation of AKT. Moreover, our study identified the talin1 rod domain to be responsible for its interaction with MyD88, which does not interfere with the interaction of talin with PIP5K through its head domain (Di Paolo et al., 2002; Ling et al., 2002). However, the PIP5K binding domain of talin potentially overlaps with the β-integrin binding site of talin. It is unclear whether talin is able to bind to integrin and PIP5K concurrently. Furthermore, upon ligand binding, we observed dissociation of talin1 from the progressively assembling TLR signalosome, which could permit the recruitment of IRAK4, one of the immediate downstream effectors, to MyD88 within TLR complexes. These spatial and temporal signaling events are likely to be critical for this novel regulatory mechanism to control proper recruitment and activation of TLR downstream signaling molecules.

Most of the fundamental mechanistic knowledge of TLR signaling pathways is derived from the analysis of macrophages or structural studies. However, our data, in conjunction with increasing evidence from other studies, suggest structural differences in TLRs expressed on DCs and macrophages. Because we observed that most of the surface TLR4 is associated with MD2 and that MyD88 recruitment requires TIRAP (MAL)-supported dimerization of TLR4 (Ve et al., 2017), the preassembled complex reported here is likely to be in a TLR4 dimer configuration, which is readily primed to become activated upon exposure to LPS. Unlike TLR8 and 9 that dimerize in solution (Manavalan et al., 2011), TLR4 and TLR2 typically exist as monomers, but could potentially dimerize at high concentrations (Xu et al., 2000). TLR4 could be expressed at a higher density on DCs than on macrophages, thereby specifically enhancing the ligand-independent dimerization of TLR4 and MyD88 recruitment in steady-state DCs.

Collectively, we have demonstrated that talin plays an important role in the initiation of TLR signaling pathways and activation of DCs. Our study represents an important conceptual shift in the preconceived idea of how TLRs function in DCs, which not only is relevant for understanding innate immune responses in the initial phase of microbial infection, but may also have long-lasting impacts on our conception of adaptive immune responses and final clearance of microbes.

Materials and methods

Mice

Tln1$^{f/f}$ mice (Petrich et al., 2007) were crossed with *CD11c*-Cre mice (Caton et al., 2007) or *Mx*-Cre mice (Kühn et al., 1995) to generate mice with talin1-deficient DCs or hematopoietic cells. All mice were bred and maintained under specific pathogen–free conditions at the animal facility of the School of Biological Sciences, Nanyang Technological University. All mouse protocols were conducted in accordance with the guidelines of the Nanyang Technological University Institutional Animal Care and Use Committee.

Epicutaneous *S. aureus* infection

S. aureus were cultured on tryptic soy agar or tryptic soy broth (Sigma-Aldrich) at 37°C overnight, followed by short-term propagation for 2–3 h in fresh tryptic soy broth to an OD_{600} of 1.8 (Montgomery et al., 2014; on the day of infection). The backs of mice were shaved, and remaining hair was chemically removed the day before infection. The stratum corneum was removed by performing 20 strokes with 240-grit sandpaper (3M) followed by application of 2×10^7 *S. aureus* particles in 50 µl of sterile PBS (Gibco). Retrospective verification by serial dilution was performed to enumerate CFUs on tryptic soy agar. The drop-plate method was used to enumerate the number of *S. aureus* on infected mice by excising and homogenizing skin lesions in PBS containing 0.1% Triton X-100, followed by plating (in triplicate) 20 µl of serially diluted skin lesion samples.

CHS and tolerance induction model

For CHS, mice were sensitized epicutaneously by painting shaved back skin with 25 µl of 0.5% DNFB (Sigma-Aldrich) or, as indicated, with a vehicle of acetone (Merck) and olive oil (Borges; 4:1, vol/vol). Mice were challenged 5 d later with the topical application of 4 µl of 0.1% DNFB onto both sides of the ears. For induction of cutaneous tolerance, 100 µl of 1.0% DNTB (Sigma-Aldrich) in acetone and olive oil was applied onto shaved abdominal skin 7 d before sensitization with 0.5% DNFB on shaved back skin, followed by ear challenge 5 d later with 0.1% DNFB. Ear swelling after 0.1% DNFB challenge was measured using a micrometer (Mitutoyo). Inguinal LNs were harvested, and cells were stained for mDCs and mLCs 2 and 3 d after DNFB sensitization, respectively, or 3 d after DNTB tolerization. Foxp3$^+$ T reg cells were detected by flow cytometry (as described below) 5 d after DNTB painting. Cytotoxic T cells were restimulated with phorbol 12,13-dibutyrate (PBDu) and calcium ionophore A23187 5 d after DNFB sensitization (Sigma-Aldrich). Treatment of mouse ears with 1.0% DNTB alone was also used to induce minor inflammation in some experiments.

Skin explant assay

Ears were split into dorsal and ventral halves and cultured in 1.5 of ml complete RPMI 1640 in 24-well tissue culture plates for 24

or 48 h at 37°C. The epidermal sheet was separated from the dermis by incubating the split ear halves in Hanks' balanced salt solution containing dispase II (Invitrogen) for 45 min at 37°C. In some experiments, the epidermal sheet was separated from the dermis before culture. For immunofluorescence analysis, the epidermal sheet was fixed in acetone for 20 min at −20°C. For flow cytometric analysis, epidermal and dermal sheets were cut into small pieces and digested in complete RPMI 1640 containing Liberase TM Research Grade (Roche) and DNase I (Roche) for 1.5 h at 37°C. Tissue fragments were then homogenized using a 1-ml syringe before filtration through a 70-µm nylon mesh to obtain a homogeneous single-cell suspension.

In vivo BrdU labeling assay

Mice were i.p. injected with 1 mg BrdU (Sigma-Aldrich) and given drinking water supplemented with 0.8 mg/ml BrdU for 7 d. Epidermal cell suspensions were generated and processed using the FITC BrdU Flow Kit (BD PharMingen).

I.d. injection of LPS

Briefly, mice were anesthetized with isoflurane. 5 µl and 200 µl of 10 µg/ml O111:B4 LPS (Sigma-Aldrich) were i.d. injected into the ear and trunk skin, respectively. Ears and sdLNs (defined as axillary, brachial, and inguinal LNs) were harvested at 24 h and 48–60 h after LPS injection, respectively. Single-cell suspensions were generated, and cells were stained for flow cytometry analysis. Epidermal sheets were also isolated and immunofluorescent staining was performed as described below.

Isolation of cells from lymphoid organs

LNs were disrupted with forceps and digested in a solution of 0.42 U/ml Liberase TM (Roche) and 0.1–0.5 mg/ml DNase I (Roche) in 10% FCS/RPMI for 30 min at 37°C. Digested tissues were triturated 8–10 times and filtered using a 100-µm cell strainer (BD Bioscience). sdLNs were defined as axillary, brachial, and inguinal, unless stated otherwise. Alternatively, LNs were harvested and cell suspensions were generated in chilled balanced salt solution (BSS; Lim et al., 2016) supplemented with 2% FCS (Biowest), if Liberase treatment was not required. To isolate cells from the skin, mouse ears were split into dorsal and ventral halves with forceps. The epidermis and dermis were separated using 1.2 mg/ml dispase II (Invitrogen). Epidermis and dermis were further digested in a solution of 0.1 mg/ml collagenase IV (Sigma-Aldrich) and 0.1–0.5 mg/ml DNase I (Roche). After digestion, both epidermal and dermal cell suspensions were triturated and filtered to remove debris. Cells from suspensions were counted and stained for FACS or flow cytometry analysis. To isolate epidermal cells from trunk skin, hair was removed by shaving before skin excision. Subcutaneous fat was removed using a scalpel, and the skin was subsequently cut into smaller pieces (2 × 2 cm) before trypsin (0.25%, Gibco) digestion for 1 h at 37°C. Epidermis from the trunk skin was scraped off using a scalpel before further digestion in a solution of collagenase IV and DNase I, as described above. Dermis was discarded. After digestion, epidermal cell suspensions were triturated and filtered to remove debris. Cells from suspensions were counted and stained for FACS or flow cytometry analysis.

Generation of BMDCs and BMDMs

BMDCs were generated using a standard protocol. Briefly, hip bones, femurs, and tibiae from poly(I)•poly(C)-treated control or *Tln1*$^{f/f}$*Mx*-Cre mice were flushed with complete RPMI. Two million BM cells/well were seeded onto 24-well plates (Thermo Fisher Scientific) in complete RPMI (Gibco) supplemented with 20 ng/ml IL-4 (PeproTech) and 2% GM-CSF conditioned medium or 10 ng/ml GM-CSF (PeproTech; Kiel et al., 2005). BM cells were gently pipetted on day 2 to remove suspended cells, with half of the existing medium replaced with fresh 2% GM-CSF conditioned medium or 10 ng/ml GM-CSF containing complete RPMI. BM cells were cultured for an additional 6 d with medium replacement every 2 d, or as required. To generate mature BMDCs, immature cells were stimulated with 100 ng/ml O111:B4 LPS overnight. To generate FMS-like tyrosine kinase 3 ligand (Flt3L)–derived BMDCs, 10^6 BM cells/well were seeded onto 24-well plates in complete RPMI supplemented with 2% Flt3L conditioned medium (Ruedl et al., 2008) and cultured for 9–10 d. BMDCs were harvested by scraping (VWR) for flow cytometry analysis. To generate BMDMs, 2 × 10^6 BM cells were seeded onto 6-well plates (Corning) in complete DMEM (GE Hyclone) supplemented with 10% L929 fibroblast cell conditioned medium containing M-CSF (Khameneh et al., 2011). Fresh L929-supplemented complete DMEM was added on day 4, and cells were cultured for an additional 3 d. BMDMs were harvested by scraping (VWR) after Accutase (Gibco) treatment for flow cytometry analysis or lysed on the plate for biochemical experiments. Under these culture conditions, we routinely generated >90% of CD11c$^+$MHC$^+$ BMDCs and F4/80$^+$Cd11b$^+$ BMDMs. BMDCs and BMDMs from control mice are defined as *Tln1*$^{f/f}$, and cells from poly(I)•poly(C)-treated *Tln1*$^{f/f}$*Mx*-Cre mice are defined as *Tln1*$^{\Delta/\Delta}$.

SiRNA transfection of BMDCs

BMDCs were transfected (Lipofectamine RNAiMax, Invitrogen) with 5 µM ON-TARGETplus SMARTpool mouse Pip5k1c siRNAs or ON-TARGETplus nontargeting control siRNAs (Horizon Discovery) and analyzed 36 to 48 h later.

Stimulation of BMDCs and BMDMs

BMDCs and BMDMs were either stimulated with 100 ng/ml O111:B4 LPS, 300 ng/ml Pam3CSK4, 100 ng/ml MALP2, and 100 ng/ml flagellin or transfected (Lipofectamine 2000, Invitrogen) with 10 µg/ml high molecular weight poly(I:C) or 1 µg/ml CpG oligodeoxynucleotide 2395 (all from InvivoGen) for the indicated times. After stimulation, cells were quenched with ice-cold PBS and lysed on the plate with radioimmunoprecipitation assay buffer (10 mM Tris-HCl, pH 8.0, 1 mM EDTA, pH 8.0, 140 mM sodium chloride, 1% Triton X-100, 0.1% SDS, and 0.1% DOC) for total lysate; Triton X-100 lysis buffer (20 mM Hepes, pH 7.4, 1% Triton X-100, 150 mM sodium chloride, 2 mM EDTA, and 1.5 mM $MgCl_2$) for IP; or cell fractionation buffers (Cell Signaling Technology) supplemented with 10 mM NaF, 10 mM Na_3VO_4, 1 mM DTT, 2% mammalian protease inhibitor cocktail, and 2 mM PMSF (all from Sigma-Aldrich). Endosomes were isolated with the Trident Endosome isolation kit (GeneTex). Samples were resolved using SDS-PAGE, transferred to a 0.2- or

0.45-µm polyvinylidene difluoride (Merck) membrane, and probed with the indicated antibodies. To study the activation of integrins in vitro, BMDCs were seeded onto fibronectin (10 µg/ml)-coated culture dishes (Corning) for 30 min at 37°C. Nonadherent cells were removed, and adherent cells were subsequently harvested.

Retroviral transduction of BMDCs

Retroviral supernatant supplemented with 5 µg/ml Polybrene (Sigma-Aldrich) was added to BMDCs 3 d after initial seeding. Room temperature spin transduction at 1,000 *g* for 1.5 h was performed. Viral supernatant was removed 1 h after spin transduction and was replaced with fresh medium. Spin transduction was also performed on day 4 of BMDC culture. Transduced BMDCs were harvested and processed on day 8.

In vitro restimulation of T cells

To determine the cytokine secretion potential of T cells, 5×10^4 to 10^5 cells from sdLNs were cultured in 96-well culture plates (Corning) and restimulated with 10 ng/ml PBDu and 500 ng/ml calcium ionophore A23187 in complete RPMI 1640 supplemented with 10 µg/ml brefeldin A (all from Sigma-Aldrich) for 5 h at 37°C. After restimulation, cells were harvested and stained for flow cytometry analysis.

Flow cytometry and phosphor-flow

Surface staining was performed according to standard protocol. Intracellular staining was performed according to the manufacturer's instructions (eBioscience or BD Biosciences). To assess the activation or phosphorylation of proteins using flow cytometry, cells were stimulated and fixed immediately in pre-chilled CytoFix (BD Bioscience) for 15 min on ice and permeabilized with ice-cold methanol (seven parts methanol to three parts sterile PBS) on ice for 15 min. Fixed cells were rehydrated with PBS and pelleted, followed by blocking with FcBlock (CD16/32, clone 93 or 2.4G2). Staining of antigens and phospho-proteins was performed according to standard protocol. The following antibodies were used for flow cytometry: CCR7 (4B12), CD3ε (124-2C11), CD4 (GK1.5, RM4-5), CD8α (53–6.7), CD11b (M1/70), CD11c (N418), CD25 (PC61), CD29 (HMβ1-1), 9EG7 (550531; BD Bioscience), CD45 (30-F11), CD45.1 (A20), CD45.2 (104), CD49f (GoH3) CD86 (GL-1), CD103 (2E7), Langerin or CD207 (eBioL31), TLR4 or CD284 (SA15-21), TLR4/MD2 (MTS510), pDCA-1 (eBio927), EpCAM or CD326 (G8.8), CXCR4 (L276F12), Foxp3 (FJK-16s), F4/80 (BM8), I-A/I-E (M5/114.15.2), inducible T cell costimulator (ICOS; E7.17G9), IFNγ (XMG1.2), TNFα (MP6-XT22), Streptavidin (all from BioLegend, unless stated otherwise); pAKT S473 (REA359), pERK T202/Y204 (REA152), F4/80 (REA126; Miltenyi Biotec); BrdU (BD PharMingen); Streptavidin (BD Bioscience), and E-cadherin or CD326 (36/E-cadherin) and IL-17 (eBio17B7; eBioscience). Acquisition of flow cytometry data were performed using a BD LSRFortessa X-20 (BD Biosciences). Flow cytometry data analysis was performed using FlowJo software (TreeStar).

Calcium flux assay

BMDCs were harvested, resuspended to a density of 5×10^6 cells/ml, and loaded with 5 µM Indo-1 AM (Invitrogen) in 0.1% FCS/RPMI for 45 min at 37°C. Cell suspensions were agitated at 10-min intervals to ensure even loading of Indo-1 AM. Cells were quenched with room temperature 0.1% FCS/RPMI, pelleted, and further stained with antibodies against surface antigens before sample acquisition. Indo-1–loaded cells were prewarmed to 37°C before acquisition. All events (500–600 events/s) for the first 30 s (baseline) were recorded before addition of stimulus (5–10 s downtime), followed by undisrupted acquisition for the remaining time. Recorded data are presented as a ratio of bound (405-nm)/free (485-nm) calcium ions, as a function of time (seconds), using FlowJo software.

Generation of BM chimeric mice

BM was harvested from hip bones, femurs, and tibiae of 8-wk-old donor mice. Total BM cells (1×10^7) were injected i.v. into lethally irradiated (5.5 Gy × 2; Eckert & Ziegler) 8-wk-old recipient mice. Recipient mice were fed with drinking water supplemented with antibiotics (neomycin, kanamycin, and gentamycin; Sigma-Aldrich) for at least 2 wk. BM chimeras were analyzed 8 wk after BM transplant.

Calcium phosphate transfection and generation of retroviral supernatant

HEK-293T cells (4×10^5 cells) were seeded onto 6-cm culture dishes and transfected the next day using standard calcium phosphate transfection protocol. Transfected cells were lysed 24 h later with supplemented Triton X-100 buffer and IP of MyD88 (Flag IP) or talin1 (GFP IP) was performed. To produce retroviral supernatant for BMDC transduction, HEK-293T cells (3×10^6 cells seeded onto 10-cm culture dishes; Corning) were transfected with 10 µg MIG-EV, MIG-GFP-talin1, MIG-GFP-talin1-W359A, or MIG-GFP-talin1-L325R with 10 µg pCL-Eco packaging plasmid (all vectors). Virus-containing supernatants were collected at 48 and 72 h, respectively, and filtered (0.45-µm unit; Pall).

ELISA

BMDCs were stimulated with the indicated compounds for 1 h before exogenous stimuli–containing supernatants were replaced with fresh complete RPMI. The duration of stimulation indicated began with the addition of exogenous stimuli. Supernatants from stimulated BMDCs were collected at 12 and 24 h, respectively, and stored at −20°C until sample collection was complete. 96-well plates were prepared for ELISA according to the manufacturer's instructions (BioLegend). Absorbance was measured using the Tecan Infinite M200 spectrophotometer (Tecan).

Western blotting

Western blotting (immunoblotting) was performed according to standard protocols. The following antibodies were used: TLR3 (6961), TLR4 (14358), MyD88 (4283), TIRAP (13077), TRIF (4596), IRAK4 (4364), TRAF3 (4729), Vav1 (4657), Vav1 (2502), p85 (4257), PIP5K1c (3296), p85 (4292), pERK1/2 T202/Y204 (4370), ERK1/2 (4695), pAKT S473 (4060), pAKT T308 (13038), pJNK1/2 T183/Y185 (9255), pp38 T180/Y182 (9211), pIRF3 S396 (4947), pIκBα S32 (2859), FAK (3285), EEA-1 (3288), pTBK1 S172 (5483),

TBK1 (3504; all from CST); CD11b M1/70 (ab184308), CD29 (ab183666), TLR9 (ab37154; all from Abcam); TLR4 (sc-293072), TLR3 (sc-32232), GFP (sc-9996), GFP (sc-8334), Vav (sc-132), MyD88 (sc-74532), MyD88 (sc-136970), Na/K ATPase (sc-21712), AKT (sc-1618), JNK1/2 (sc-7345), p38 (sc-7972), IRF3 (sc-376455), lamin B1 (sc-374015), p65 (sc-109), CD29 (sc-8978), IκBα (sc-1643; all from Santa Cruz Biotechnology); TRAM (AF4348; R&D Biosystems), TRAF6 (GTX113029; GeneTex), Talin1 (T3287), Flag M2 (F3165 and F7425; both from Sigma-Aldrich); GAPDH (AM4300), IRAK4 (700026), and TLR4 (48–2300; all from Invitrogen).

IP

BMDCs were stimulated with 100 ng/ml O111:B4 LPS (TLR4 IP) for 30 min or transfected with 10 µg/ml high molecular weight poly(I:C) (TLR3 IP) for 45 min. BMDMs were stimulated with 100 ng/ml O111:B4 LPS (TLR4 IP) for 30 min. After stimulation, cells were quenched with ice-cold PBS and harvested by scraping (VWR). Harvested cells were lysed in supplemented Triton X-100 lysis buffer or fractionated into membrane and cytosolic fractions (Cell Fractionation Kit, CST) according to the manufacturer's instructions. Fractions and samples were precleared with protein G sepharose beads (GE Healthcare) for 30 min at 4°C. TLR4 (sc-293072, Santa Cruz Biotechnology, or 14358, CST) or TLR3 (sc-52961; Santa Cruz Biotechnology) antibody was added, and samples were further incubated overnight at 4°C. Protein G sepharose beads were added, and samples were incubated for 3 h at 4°C. Subsequently, antibody-bound beads were washed 3 times with Triton X-100 buffer and boiled in 2× Laemmli buffer (Bio-Rad). Samples were resolved on SDS-PAGE, and immunoblotting was performed using the indicated antibodies. Other antibodies used for IP included 9EG7 (553715; BD Bioscience); MyD88 (13077; CST); Talin1 (T3287), Flag (F3165 and F7425; all from Sigma-Aldrich); GFP (sc-9996 and sc-8334), MyD88 (sc-74532 and sc-136970; all from Santa Cruz Biotechnology); CD29 (ab1843080), CD11b (ab183666), and TLR9 (ab37154; all from Abcam).

In vitro transcription/translation (IVT) assay

IVT or cell-free protein expression assays (Invitrogen) were performed according to the manufacturer's instructions. Translated proteins were incubated in a 1:1 (vol/vol) ratio overnight before IP was performed using anti-MyD88, anti-talin1, or anti-Vav1 antibodies. Subsequently, antibody-bound beads were washed three times with Triton X-100 buffer and boiled in 2× Laemmli buffer. Samples were resolved on SDS-PAGE, and immunoblotting was performed using the indicated antibodies.

Reverse transcription quantitative real-time PCR (RT-qPCR)

Total RNA from cells and tissues was extracted using TRIzol (Invitrogen), and complementary DNA was reversed transcribed using Superscript Reverse Transcription (Invitrogen). Primers were designed or retrieved from PrimerBank (Harvard Medical School) to amplify specific genes. mRNAs were quantitated by RT-qPCR using IQ SYBR Green Supermix (Bio-Rad) according to the manufacturer's instructions. Data were normalized to *Gapdh* and expressed as the fold change relative to control. Primers: *Fermt3* forward (F), 5′-ATGGCGGGTATGAAGACAGC-3′; *Fermt3* reverse (R), 5′-CACCAATGTGCGACTCCCC-3′; *Tln2* F, 5′-ATG GTGGCCCTATCCTTAAAGA-3′; *Tln2* R, 5′-TGACTCGACAAGCGT CATACA-3′; *Mmp2* F, 5′-CAAGTTCCCCGGCGATGTC-3′; *Mmp2* R, 5′-TTCTGGTCAAGGTCACCTGTC-3′; *Mmp9* F, 5′-CTGGACAGC CAGACACTAAAG-3′; *Mmp9* R, 5′-CTCGCGGCAAGTCTTCAGAG-3′; *Gapdh* F, 5′-ATCTTTTGGGGTCCGTCAACT-3′; *Gapdh* R, 5′-TTTGCACTGGTACGTGTTGAT-3′; *Il1b* F, 5′-GCAACTGTTCCT GAACTCAACT-3′; *Il1b* R, 5′-ATCTTTTGGGGTCCGTCAACT-3′; *Tnfa* F, 5′-CCCTCACACTCAGATCATCTTCT-3′; *Tnfa* R, 5′-GCT ACGACGTGGGCTACAG-3′; *Il23a* F, 5′-ATGCTGGATTGCAGA GCAGTA-3′; *Il23a* R, 5′-ACGGGGCACATTATTTTTAGTCT-3′; *Il6* F, 5′-CTCGCGGCAAGTCTTCAGAG-3′; *Il6* R, 5′-CTGTTGTTCAGA CTCTCTCCCT-3′; *Ifnb1* F, 5′-CAGCTCCAAGAAAGGACGAAC-3′; *Ifnb1* R, 5′-GGCAGTGTAACTCTTCTGCAT-3′.

Epidermal sheet microscopy

Mouse ears were split into dorsal and ventral halves with forceps and floated on 0.5 M ammonium thiocyanate (Sigma-Aldrich) in PBS at 37°C for 40 min. Isolated sheets were then fixed in ice-cold acetone (Merck) for 10 min, rinsed with PBS, blocked in 1% BSA/PBS for 1 h at room temperature, and stained with anti-I-A/I-E antibody (BioLegend) overnight. After staining, sheets were mounted with Fluoromount aqueous mounting medium (Sigma-Aldrich) or ProLong Gold AntiFade Mountant (Invitrogen) containing DAPI (Invitrogen). Images were acquired with a Nikon fluorescence microscope using Metamorph (Molecular Devices). Captured images were analyzed and processed with Fiji.

Confocal microscopy

BMDCs were seeded onto µ-slide $IV^{0.4}$ (Ibidi) for 30 min and fixed using prewarmed BD Cytofix (BD Bioscience) for 15 min at room temperature or 37°C. Fixed cells were incubated with 0.5% ice-cold Triton X-100 (Sigma-Aldrich) on ice for 5 min and washed three times with BD Cytoperm (BD Bioscience). Blocking with 5% donkey/5% goat serum (Sigma-Aldrich)/Cytoperm was performed for 1 h at room temperature. Cells were stained overnight with anti-talin1 (Sigma-Aldrich), anti-TIRAP (CST), anti-MyD88 (3244R, Bio-vision, or 4283, CST), anti-PIP2 (ADI-915-062, Assay Diagnostics, currently Enzo Life Sciences) or anti-TLR4/MD2 ($TLR4^{MD2}$) biotin or PE conjugate (clone MTS510, 117605, and 117603, BioLegend), or anti-TLR4 (clone SA15-21, 145401, BioLegend) in 0.5% donkey/0.5% goat serum/Cytoperm. Primary antibody–stained cells were washed three times with PBS followed by further incubation with secondary antibodies (Jackson ImmunoResearch) or streptavidin (BioLegend) in 0.5% donkey/0.5% goat serum/Cytoperm for 1 h at room temperature. Secondary antibody–stained cells were washed five times with PBS, mounted with ProLong Gold or Diamond Antifade Mountant with DAPI (Invitrogen), and visualized with an LSM 710 with airyscan (Zeiss). To visualize PIP2 clusters in DCs, cells were stained in 96-well plates and adhered onto glass slides by cytospin at 600 rpm for 3 min (Thermo Fisher Scientific). Captured images were processed with Zen microscope software (Zeiss) or ImageJ/Fiji.

Image analysis

Pixel intensity spatial correlation of two monochromatic 8-bit images was analyzed using ImageJ/Fiji plugin Coloc 2 to generate Spearman's correlation coefficients (Colocalization index, *r*). To analyze the colocalization of proteins in three fluorochromatic channels, an arbitrary pixel threshold of each fluorochromatic channel was defined and used across all images in all experiments, followed by the conversion of images to binary masks. To generate triple colocalization images, double colocalization images were overlaid with an image depicting the third protein of interest. Colocalization of binary images was also analyzed using ImageJ plugin Coloc 2. Colocalized images were generated by Image Calculator plugin (ImageJ/Fiji) using operator AND. Inverted double and triple colocalization images are displayed.

Live-cell imaging

BMDCs were embedded into bovine collagen type I matrix (1.6 mg/ml; Advanced BioMatrix) and introduced to a µ-slide chemotaxis chamber (Ibidi) according to the manufacturer's instructions. Various concentrations of the chemokine CCL19 (Peprotech) in 2% FCS/RPMI were added to the chamber upon solidification of the collagen matrix (37°C for 45 min). Live-cell imaging (5% CO_2, 37°C) was performed immediately using a Nikon microscope. Time-lapse images (2- to 3-min intervals between images) were acquired using Metamorph (Molecular Devices). Captured images were processed using the chemotaxis plugin (ImageJ/Fiji).

Skin histology

Skin samples were excised and fixed in 2% paraformaldehyde in 30% sucrose overnight at 4°C before embedding in optimal cutting temperature compound (Tissue-Tek) and sectioned. Frozen skin sections were dehydrated in ethanol and xylene after H&E staining. Skin epidermal thickness was quantified using ImageJ/Fiji.

Statistics

Statistical significance was determined using the two-tailed Student's *t* test and Spearman's correlation coefficient and defined as follows: *, $0.01 < P \leq 0.05$; **, $0.005 < P \leq 0.01$; and ***, $0.001 < P \leq 0.005$. Bar graphs are the mean ± SD of combined experiments and group sizes, as indicated in the figure legends. SD is not indicated in scatter bar charts to enhance the clarity of data presentation. SEM was used for the ear thickness measurements. The Wilcoxon signed-rank test was used to determine statistical differences in the numbers and sizes of TIRAP/PIP2 clusters between groups. Figures were prepared using Prism 6 or 7 (GraphPad Software) and Illustrator (Adobe).

Online supplemental material

Fig. S1 shows accumulation of talin1-deficient LCs in epidermis and reduced migration of talin1-deficient BMDCs. Fig. S2 demonstrates talin1-regulated DC activation. Fig. S3 characterizes LPS-promoted activation of BMDCs derived from Flt3L or GM-CSF cultures. Fig. S4 reveals the requirement of talin1 in BMDMs despite lacking preassembled TLR4 complexes. Fig. S5 displays prominent preassembled TLR4 complexes in BMDCs and not BMDMs.

Acknowledgments

We thank B.G. Petrich (Emory University, Atlanta, GA) for providing the talin1-conditional knockout mice and A*STAR Biological Resource Centre for providing the *CD11c*-Cre mice. We thank C. Ruedl and K.E. Karjalainen (Nanyang Technological University) for discussions and suggestions. We thank S.K. Lai (Nanyang Technological University) for her superb guidance in confocal and airyscan microscopy. We thank K. Kline (Nanyang Technological University) for providing *S. aureus* USA300Lac strain. We thank Caris Tan (National University of Singapore Life Sciences Institute Histology Core) for preparing mouse skin sections. We also thank A. Sullivan from Obrizus Communications for critical reading and editing of the manuscript.

This work was supported by the Agency for Science, Technology and Research (A*STAR) Graduate Academy (to T.J.F. Lim); the Ministry of Health - Singapore Academic Research Fund Tier 1 RG36/17, Tier 2 MOE2013-T2-2-038, and MOE2017-T2-2-054; and the Ministry of Health - Singapore, National Medical Research Council NMRC-OFIRG 18may-0024 (to I. Su).

Author contributions: T.J.F. Lim designed and conducted most of the experiments, interpreted data, and was involved in manuscript preparation. M. Bunjamin performed some experiments. C. Ruedl provided reagents, technical support, and scientific discussion. I. Su designed and interpreted the experiments and wrote the manuscript.

Disclosures: The authors declare no competing interests exist.

Submitted: 26 September 2019
Revised: 24 February 2020
Accepted: 27 March 2020

References

Anthis, N.J., K.L. Wegener, D.R. Critchley, and I.D. Campbell. 2010. Structural diversity in integrin/talin interactions. *Structure*. 18:1654–1666. https://doi.org/10.1016/j.str.2010.09.018

Bai, Y., C. Qian, L. Qian, F. Ma, J. Hou, Y. Chen, Q. Wang, and X. Cao. 2012. Integrin CD11b negatively regulates TLR9-triggered dendritic cell cross-priming by upregulating microRNA-146a. *J. Immunol.* 188:5293–5302. https://doi.org/10.4049/jimmunol.1102371

Berridge, M.J.. 1993. Inositol trisphosphate and calcium signalling. *Nature*. 361:315–325. https://doi.org/10.1038/361315a0

Bovay, E., A. Sabine, B. Prat-Luri, S. Kim, K. Son, A.H. Willrodt, C. Olsson, C. Halin, F. Kiefer, C. Betsholtz, et al. 2018. Multiple roles of lymphatic vessels in peripheral lymph node development. *J. Exp. Med.* 215: 2760–2777. https://doi.org/10.1084/jem.20180217

Burns, K., S. Janssens, B. Brissoni, N. Olivos, R. Beyaert, and J. Tschopp. 2003. Inhibition of interleukin 1 receptor/Toll-like receptor signaling through the alternatively spliced, short form of MyD88 is due to its failure to recruit IRAK-4. *J. Exp. Med.* 197:263–268. https://doi.org/10.1084/jem.20021790

Calderwood, D.A., I.D. Campbell, and D.R. Critchley. 2013. Talins and kindlins: partners in integrin-mediated adhesion. *Nat. Rev. Mol. Cell Biol.* 14: 503–517. https://doi.org/10.1038/nrm3624

Caton, M.L., M.R. Smith-Raska, and B. Reizis. 2007. Notch-RBP-J signaling controls the homeostasis of CD8- dendritic cells in the spleen. *J. Exp. Med.* 204:1653–1664. https://doi.org/10.1084/jem.20062648

Chinthalapudi, K., E.S. Rangarajan, and T. Izard. 2018. The interaction of talin with the cell membrane is essential for integrin activation and focal adhesion formation. *Proc. Natl. Acad. Sci. USA*. 115:10339–10344. https://doi.org/10.1073/pnas.1806275115

Clausen, B.E., and P. Stoitzner. 2015. Functional Specialization of Skin Dendritic Cell Subsets in Regulating T Cell Responses. *Front. Immunol.* 6:534. https://doi.org/10.3389/fimmu.2015.00534

Di Paolo, G., L. Pellegrini, K. Letinic, G. Cestra, R. Zoncu, S. Voronov, S. Chang, J. Guo, M.R. Wenk, and P. De Camilli. 2002. Recruitment and regulation of phosphatidylinositol phosphate kinase type 1 gamma by the FERM domain of talin. *Nature*. 420:85–89. https://doi.org/10.1038/nature01147

Dong, G., Y. Wang, W. Xiao, S. Pacios Pujado, F. Xu, C. Tian, E. Xiao, Y. Choi, and D.T. Graves. 2015. FOXO1 regulates dendritic cell activity through ICAM-1 and CCR7. *J. Immunol.* 194:3745–3755. https://doi.org/10.4049/jimmunol.1401754

Eisenbarth, S.C.. 2019. Dendritic cell subsets in T cell programming: location dictates function. *Nat. Rev. Immunol.* 19:89–103. https://doi.org/10.1038/s41577-018-0088-1

Faure-André, G., P. Vargas, M.-I. Yuseff, M. Heuzé, J. Diaz, D. Lankar, V. Steri, J. Manry, S. Hugues, F. Vascotto, et al. 2008. Regulation of dendritic cell migration by CD74, the MHC class II-associated invariant chain. *Science*. 322:1705–1710. https://doi.org/10.1126/science.1159894

Gay, N.J., M.F. Symmons, M. Gangloff, and C.E. Bryant. 2014. Assembly and localization of Toll-like receptor signalling complexes. *Nat. Rev. Immunol.* 14:546–558. https://doi.org/10.1038/nri3713

Gomez de Agüero, M., M. Vocanson, F. Hacini-Rachinel, M. Taillardet, T. Sparwasser, A. Kissenpfennig, B. Malissen, D. Kaiserlian, and B. Dubois. 2012. Langerhans cells protect from allergic contact dermatitis in mice by tolerizing CD8(+) T cells and activating Foxp3(+) regulatory T cells. *J. Clin. Invest.* 122:1700–1711. https://doi.org/10.1172/JCI59725

Gunawan, M., N. Venkatesan, J.T. Loh, J.F. Wong, H. Berger, W.H. Neo, L.Y. Li, M.K. La Win, Y.H. Yau, T. Guo, et al. 2015. The methyltransferase Ezh2 controls cell adhesion and migration through direct methylation of the extranuclear regulatory protein talin. *Nat. Immunol.* 16:505–516. https://doi.org/10.1038/ni.3125

Han, C., J. Jin, S. Xu, H. Liu, N. Li, and X. Cao. 2010. Integrin CD11b negatively regulates TLR-triggered inflammatory responses by activating Syk and promoting degradation of MyD88 and TRIF via Cbl-b. *Nat. Immunol.* 11:734–742. https://doi.org/10.1038/ni.1908

Jakob, T., and M.C. Udey. 1998. Regulation of E-cadherin-mediated adhesion in Langerhans cell-like dendritic cells by inflammatory mediators that mobilize Langerhans cells in vivo. *J. Immunol.* 160:4067–4073.

Jiang, A., O. Bloom, S. Ono, W. Cui, J. Unternaehrer, S. Jiang, J.A. Whitney, J. Connolly, J. Banchereau, and I. Mellman. 2007. Disruption of E-cadherin-mediated adhesion induces a functionally distinct pathway of dendritic cell maturation. *Immunity*. 27:610–624. https://doi.org/10.1016/j.immuni.2007.08.015

Kabashima, K., N. Shiraishi, K. Sugita, T. Mori, A. Onoue, M. Kobayashi, J. Sakabe, R. Yoshiki, H. Tamamura, N. Fujii, et al. 2007. CXCL12-CXCR4 engagement is required for migration of cutaneous dendritic cells. *Am. J. Pathol.* 171:1249–1257. https://doi.org/10.2353/ajpath.2007.070225

Kagan, J.C., and R. Medzhitov. 2006. Phosphoinositide-mediated adaptor recruitment controls Toll-like receptor signaling. *Cell*. 125:943–955. https://doi.org/10.1016/j.cell.2006.03.047

Kaplan, D.H.. 2017. Ontogeny and function of murine epidermal Langerhans cells. *Nat. Immunol.* 18:1068–1075. https://doi.org/10.1038/ni.3815

Kashem, S.W., B.Z. Igyarto, M. Gerami-Nejad, Y. Kumamoto, J.A. Mohammed, E. Jarrett, R.A. Drummond, S.M. Zurawski, G. Zurawski, J. Berman, et al. 2015. Candida albicans morphology and dendritic cell subsets determine T helper cell differentiation. *Immunity*. 42:356–366. https://doi.org/10.1016/j.immuni.2015.01.008

Kawasaki, T., and T. Kawai. 2014. Toll-like receptor signaling pathways. *Front. Immunol.* 5:461. https://doi.org/10.3389/fimmu.2014.00461

Kel, J.M., M.J. Girard-Madoux, B. Reizis, and B.E. Clausen. 2010. TGF-beta is required to maintain the pool of immature Langerhans cells in the epidermis. *J. Immunol.* 185:3248–3255. https://doi.org/10.4049/jimmunol.1000981

Khameneh, H.J., S.A. Isa, L. Min, F.W. Nih, and C. Ruedl. 2011. GM-CSF signalling boosts dramatically IL-1 production. *PLoS One*. 6. e23025. https://doi.org/10.1371/journal.pone.0023025

Kiel, M.J., O.H. Yilmaz, T. Iwashita, O.H. Yilmaz, C. Terhorst, and S.J. Morrison. 2005. SLAM family receptors distinguish hematopoietic stem and progenitor cells and reveal endothelial niches for stem cells. *Cell*. 121:1109–1121. https://doi.org/10.1016/j.cell.2005.05.026

King, J.K., R.L. Philips, A.U. Eriksson, P.J. Kim, R.C. Halder, D.J. Lee, and R.R. Singh. 2015. Langerhans cells maintain local tissue tolerance in a model of systemic autoimmune disease. *J. Immunol.* 195:464–476. https://doi.org/10.4049/jimmunol.1402735

Kühn, R., F. Schwenk, M. Aguet, and K. Rajewsky. 1995. Inducible gene targeting in mice. *Science*. 269:1427–1429. https://doi.org/10.1126/science.7660125

Lämmermann, T., B.L. Bader, S.J. Monkley, T. Worbs, R. Wedlich-Söldner, K. Hirsch, M. Keller, R. Förster, D.R. Critchley, R. Fässler, et al. 2008. Rapid leukocyte migration by integrin-independent flowing and squeezing. *Nature*. 453:51–55. https://doi.org/10.1038/nature06887

Larsen, C.P., R.M. Steinman, M. Witmer-Pack, D.F. Hankins, P.J. Morris, and J.M. Austyn. 1990. Migration and maturation of Langerhans cells in skin transplants and explants. *J. Exp. Med.* 172:1483–1493. https://doi.org/10.1084/jem.172.5.1483

Lim, T.J.F., and I.H. Su. 2018. Talin1 methylation is required for neutrophil infiltration and lipopolysaccharide-induced lethality. *J. Immunol.* 201:3651–3661. https://doi.org/10.4049/jimmunol.1800567

Lim, J.F., H. Berger, and I.H. Su. 2016. Isolation and activation of murine lymphocytes. *J. Vis. Exp.* doi:10.3791/54596.. https://doi.org/10.3791/54596

Lin, S.C., Y.C. Lo, and H. Wu. 2010. Helical assembly in the MyD88-IRAK4-IRAK2 complex in TLR/IL-1R signalling. *Nature*. 465:885–890. https://doi.org/10.1038/nature09121

Ling, G.S., J. Bennett, K.J. Woollard, M. Szajna, L. Fossati-Jimack, P.R. Taylor, D. Scott, G. Franzoso, H.T. Cook, and M. Botto. 2014. Integrin CD11b positively regulates TLR4-induced signalling pathways in dendritic cells but not in macrophages. *Nat. Commun.* 5:3039. https://doi.org/10.1038/ncomms4039

Ling, K., R.L. Doughman, A.J. Firestone, M.W. Bunce, and R.A. Anderson. 2002. Type I γ phosphatidylinositol phosphate kinase targets and regulates focal adhesions. *Nature*. 420:89–93. https://doi.org/10.1038/nature01082

Loh, J.T., T.J.F. Lim, K. Ikumi, T. Matoba, B. Janela, M. Gunawan, T. Toyama, M. Bunjamin, L.G. Ng, M. Poidinger, et al. 2018. Ezh2 controls skin tolerance through distinct mechanisms in different subsets of skin dendritic cells. *iScience*. 10:23–39. https://doi.org/10.1016/j.isci.2018.11.019

Malissen, B., S. Tamoutounour, and S. Henri. 2014. The origins and functions of dendritic cells and macrophages in the skin. *Nat. Rev. Immunol.* 14:417–428. https://doi.org/10.1038/nri3683

Manavalan, B., S. Basith, and S. Choi. 2011. Similar structures but different roles – an updated perspective on TLR structures. *Front. Physiol.* 2:41. https://doi.org/10.3389/fphys.2011.00041

Manevich-Mendelson, E., V. Grabovsky, S.W. Feigelson, G. Cinamon, Y. Gore, G. Goverse, S.J. Monkley, R. Margalit, D. Melamed, R.E. Mebius, et al. 2010. Talin1 is required for integrin-dependent B lymphocyte homing to lymph nodes and the bone marrow but not for follicular B-cell maturation in the spleen. *Blood*. 116:5907–5918. https://doi.org/10.1182/blood-2010-06-293506

Manning, B.D., and A. Toker. 2017. AKT/PKB signaling: Navigating the network. *Cell*. 169:381–405. https://doi.org/10.1016/j.cell.2017.04.001

Merad, M., F. Ginhoux, and M. Collin. 2008. Origin, homeostasis and function of Langerhans cells and other langerin-expressing dendritic cells. *Nat. Rev. Immunol.* 8:935–947. https://doi.org/10.1038/nri2455

Montgomery, C.P., M. Daniels, F. Zhao, M.L. Alegre, A.S. Chong, and R.S. Daum. 2014. Protective immunity against recurrent Staphylococcus aureus skin infection requires antibody and interleukin-17A. *Infect. Immun.* 82:2125–2134. https://doi.org/10.1128/IAI.01491-14

Noordegraaf, M., V. Flacher, P. Stoitzner, and B.E. Clausen. 2010. Functional redundancy of Langerhans cells and Langerin+ dermal dendritic cells in contact hypersensitivity. *J. Invest. Dermatol.* 130:2752–2759. https://doi.org/10.1038/jid.2010.223

O'Neill, L.A., and A.G. Bowie. 2007. The family of five: TIR-domain-containing adaptors in Toll-like receptor signalling. *Nat. Rev. Immunol.* 7:353–364. https://doi.org/10.1038/nri2079

Ohl, L., M. Mohaupt, N. Czeloth, G. Hintzen, Z. Kiafard, J. Zwirner, T. Blankenstein, G. Henning, and R. Förster. 2004. CCR7 governs skin dendritic cell migration under inflammatory and steady-state conditions. *Immunity*. 21:279–288. https://doi.org/10.1016/j.immuni.2004.06.014

Park, B.S., D.H. Song, H.M. Kim, B.-S. Choi, H. Lee, and J.O. Lee. 2009. The structural basis of lipopolysaccharide recognition by the TLR4-MD-2 complex. *Nature*. 458:1191–1195. https://doi.org/10.1038/nature07830

Park, H., and J. Doh. 2019. T cell migration in microchannels densely packed with T cells. *Sci. Rep.* 9:7198. https://doi.org/10.1038/s41598-019-43569-w

Petrich, B.G., P. Marchese, Z.M. Ruggeri, S. Spiess, R.A.M. Weichert, F. Ye, R. Tiedt, R.C. Skoda, S.J. Monkley, D.R. Critchley, et al. 2007. Talin is required for integrin-mediated platelet function in hemostasis and thrombosis. *J. Exp. Med.* 204:3103–3111. https://doi.org/10.1084/jem.20071800

Price, A.A., M. Cumberbatch, I. Kimber, and A. Ager. 1997. Alpha 6 integrins are required for Langerhans cell migration from the epidermis. *J. Exp. Med.* 186:1725–1735. https://doi.org/10.1084/jem.186.10.1725

Price, J.G., J. Idoyaga, H. Salmon, B. Hogstad, C.L. Bigarella, S. Ghaffari, M. Leboeuf, and M. Merad. 2015. CDKN1A regulates Langerhans cell survival and promotes Treg cell generation upon exposure to ionizing irradiation. *Nat. Immunol.* 16:1060–1068. https://doi.org/10.1038/ni.3270

Prole, D.L., and C.W. Taylor. 2019. Structure and function of IP3 receptors. *Cold Spring Harb. Perspect. Biol.* 11. a035063. https://doi.org/10.1101/cshperspect.a035063

Ratzinger, G., P. Stoitzner, S. Ebner, M.B. Lutz, G.T. Layton, C. Rainer, R.M. Senior, J.M. Shipley, P. Fritsch, G. Schuler, et al. 2002. Matrix metalloproteinases 9 and 2 are necessary for the migration of Langerhans cells and dermal dendritic cells from human and murine skin. *J. Immunol.* 168:4361–4371. https://doi.org/10.4049/jimmunol.168.9.4361

Renkawitz, J., K. Schumann, M. Weber, T. Lämmermann, H. Pflicke, M. Piel, J. Polleux, J.P. Spatz, and M. Sixt. 2009. Adaptive force transmission in amoeboid cell migration. *Nat. Cell Biol.* 11:1438–1443. https://doi.org/10.1038/ncb1992

Ruedl, C., H.J. Khameneh, and K. Karjalainen. 2008. Manipulation of immune system via immortal bone marrow stem cells. *Int. Immunol.* 20:1211–1218. https://doi.org/10.1093/intimm/dxn079

Shi, M., J. Zhu, R. Wang, X. Chen, L. Mi, T. Walz, and T.A. Springer. 2011. Latent TGF-β structure and activation. *Nature.* 474:343–349. https://doi.org/10.1038/nature10152

Thammavongsa, V., H.K. Kim, D. Missiakas, and O. Schneewind. 2015. Staphylococcal manipulation of host immune responses. *Nat. Rev. Microbiol.* 13:529–543. https://doi.org/10.1038/nrmicro3521

Tong, S.Y.C., J.S. Davis, E. Eichenberger, T.L. Holland, and V.G. Fowler, Jr.. 2015. Staphylococcus aureus infections: epidemiology, pathophysiology, clinical manifestations, and management. *Clin. Microbiol. Rev.* 28:603–661. https://doi.org/10.1128/CMR.00134-14

Vargas, P., P. Maiuri, M. Bretou, P.J. Sáez, P. Pierobon, M. Maurin, M. Chabaud, D. Lankar, D. Obino, E. Terriac, et al. 2016. Innate control of actin nucleation determines two distinct migration behaviours in dendritic cells. *Nat. Cell Biol.* 18:43–53. https://doi.org/10.1038/ncb3284

Ve, T., P.R. Vajjhala, A. Hedger, T. Croll, F. DiMaio, S. Horsefield, X. Yu, P. Lavrencic, Z. Hassan, G.P. Morgan, et al. 2017. Structural basis of TIR-domain-assembly formation in MAL- and MyD88-dependent TLR4 signaling. *Nat. Struct. Mol. Biol.* 24:743–751. https://doi.org/10.1038/nsmb.3444

Wang, J., X. Dong, B. Zhao, J. Li, C. Lu, and T.A. Springer. 2017. Atypical interactions of integrin $\alpha_V\beta_8$ with pro-TGF-β1. *Proc. Natl. Acad. Sci. USA.* 114:E4168–E4174. https://doi.org/10.1073/pnas.1705129114

Wegener, K.L., A.W. Partridge, J. Han, A.R. Pickford, R.C. Liddington, M.H. Ginsberg, and I.D. Campbell. 2007. Structural basis of integrin activation by talin. *Cell.* 128:171–182. https://doi.org/10.1016/j.cell.2006.10.048

Wernimont, S.A., A.J. Wiemer, D.A. Bennin, S.J. Monkley, T. Ludwig, D.R. Critchley, and A. Huttenlocher. 2011. Contact-dependent T cell activation and T cell stopping require talin1. *J. Immunol.* 187:6256–6267. https://doi.org/10.4049/jimmunol.1102028

Wong, K.F., J.M. Luk, R.H. Cheng, L.B. Klickstein, and S.T. Fan. 2007. Characterization of two novel LPS-binding sites in leukocyte integrin betaA domain. *FASEB J.* 21:3231–3239. https://doi.org/10.1096/fj.06-7579com

Worbs, T., S.I. Hammerschmidt, and R. Förster. 2017. Dendritic cell migration in health and disease. *Nat. Rev. Immunol.* 17:30–48. https://doi.org/10.1038/nri.2016.116

Xu, Y., X. Tao, B. Shen, T. Horng, R. Medzhitov, J.L. Manley, and L. Tong. 2000. Structural basis for signal transduction by the Toll/interleukin-1 receptor domains. *Nature.* 408:111–115. https://doi.org/10.1038/35040600

Yago, T., B.G. Petrich, N. Zhang, Z. Liu, B. Shao, M.H. Ginsberg, and R.P. McEver. 2015. Blocking neutrophil integrin activation prevents ischemia-reperfusion injury. *J. Exp. Med.* 212:1267–1281. https://doi.org/10.1084/jem.20142358

Ye, X., M.A. McLean, and S.G. Sligar. 2016. Phosphatidylinositol 4,5-bisphosphate modulates the affinity of talin-1 for phospholipid bilayers and activates its autoinhibited form. *Biochemistry.* 55:5038–5048. https://doi.org/10.1021/acs.biochem.6b00497

Zhang, Y., and H. Wang. 2012. Integrin signalling and function in immune cells. *Immunology.* 135:268–275. https://doi.org/10.1111/j.1365-2567.2011.03549.x

Supplemental material

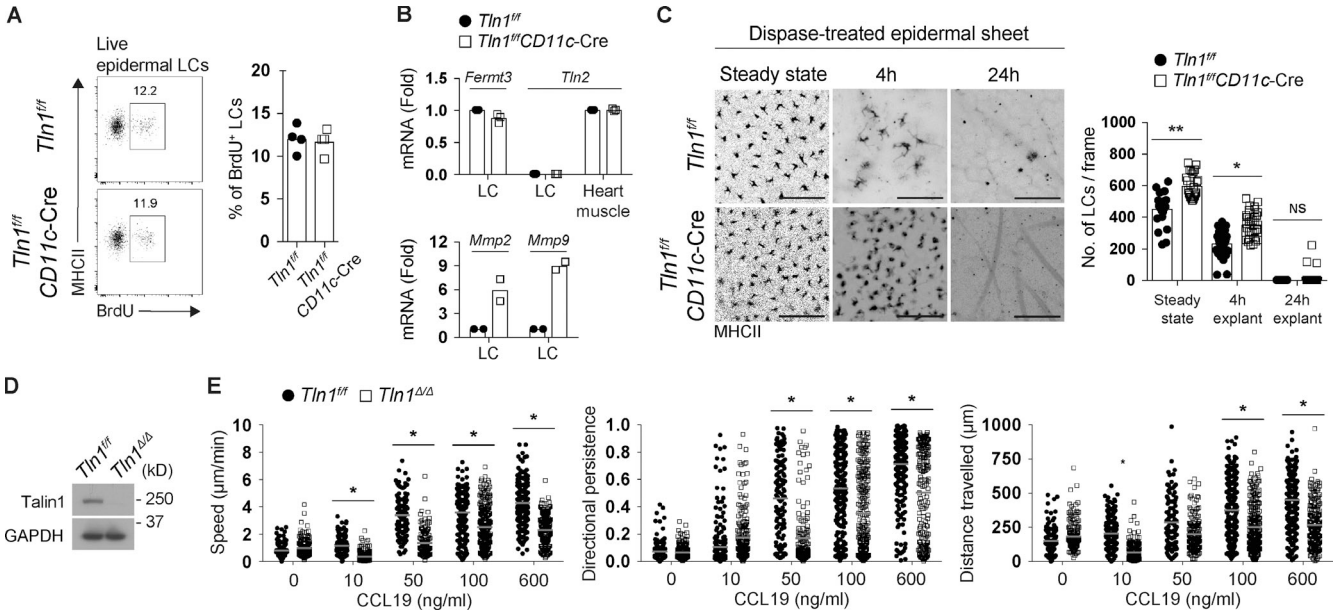

Figure S1. **Accumulation of talin1-deficient LCs in epidermis is caused by impaired integrin-dependent migration, not defective chemotaxis. (A)** Flow cytometric analysis (left) and quantification (right) of BrdU$^+$ LCs isolated from the ears of BrdU-treated control (*Tln1*$^{f/f}$) and *Tln1*$^{f/f}$*CD11c*-Cre mice. Four independent experiments (n = 4 mice/group). **(B)** Fold mRNA expression, as determined by RT-qPCR, of *Fermt3*, *Tln2*, *Mmp2*, and *Mmp9* in wild-type and talin1-deficient LCs isolated and FACS-sorted from epidermal ear sheets or heart muscle (positive control for *Tln2* expression) of corresponding mice. Two independent experiments (n = 2 mice/group). **(C)** Immunofluorescence analysis (left) and quantification (right) of LCs on dispase-treated epidermal ear sheets isolated from *Tln1*$^{f/f}$ and *Tln1*$^{f/f}$*CD11c*-Cre mice and cultured for 4 and 24 h. LCs were identified by MHCII staining; five images/ear/mouse. Scale bars, 40 µm. Three independent experiments (n = 3–6 mice/group) **(D)** Immunoblot analysis of talin1 and GAPDH (loading control) protein expression in wild-type and talin1-deficient (*Tln1*$^{\Delta/\Delta}$) BMDCs. **(E)** Scatter plot analysis of cell speed, directional persistence, and distance traveled of chemotaxing wild-type and talin1-deficient BMDCs toward CCL19 in collagen matrices. BMDCs were generated from the BM cells of poly(I)•poly(C)-treated *Tln1*$^{f/f}$ and *Tln1*$^{f/f}$*Mx*-Cre mice, as described in Fig. 1 F. 115–256 cells pooled from five independent experiments were scored. Each data point in the scatter plots indicates the cell number from one mouse (A), the fold change of target gene expression from one mouse (B), the cell number from one image (C), or the behavior of one cell (E). Data are representative (A–C) or summaries of two (B), three (A–C; mean ± SD), or five (D and E) independent experiments. Red horizontal bars in D indicate means. *, 0.01 < P ≤ 0.05; **, 0.005 < P ≤ 0.01 (two-tailed Student's t test).

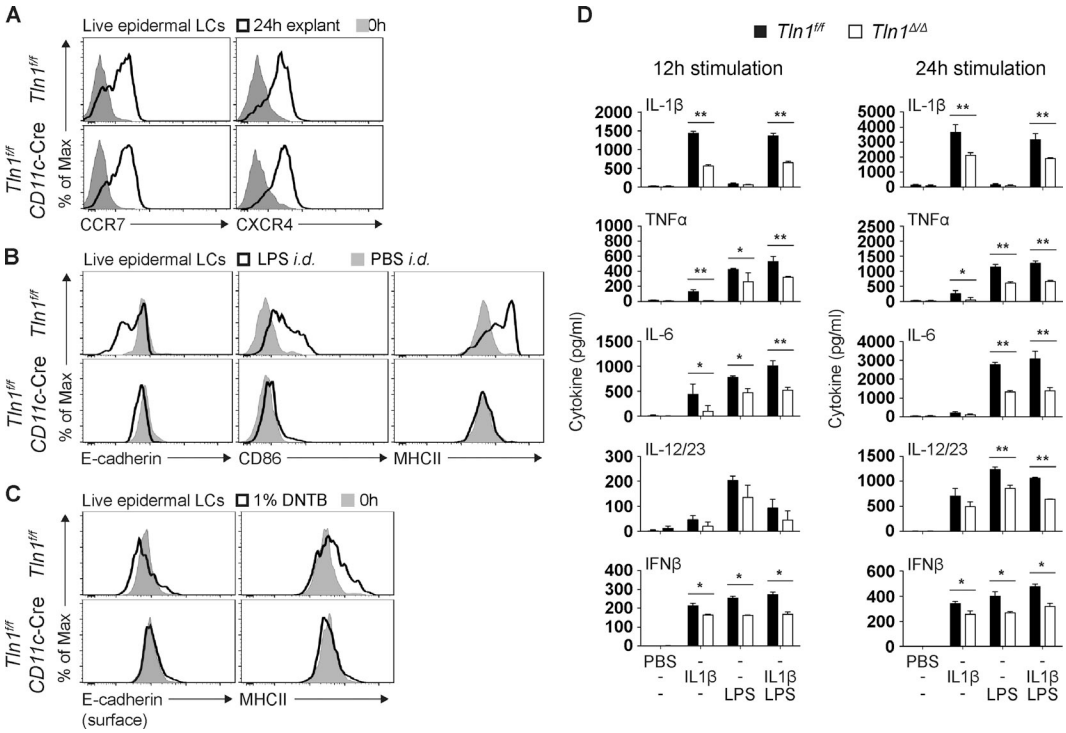

Figure S2. **Talin1 controls DC activation. (A–C)** Flow cytometric analysis of the indicated molecules in wild-type control (*Tln1*$^{f/f}$) and talin1-deficient (*Tln1*$^{f/f}$*CD11c*-Cre) LCs isolated from the epidermis of 24-h-cultured ear explants (A) or the epidermis of mouse ears i.d. injected with LPS (B) or painted with 1% DNTB (C). Four independent experiments (n = 4–6 mice/group). **(D)** ELISA results for the indicated cytokines in the supernatants produced by control or talin1-deficient BMDCs stimulated with IL-1β, LPS, or both molecules for 12 or 24 h (mean ± SD). BMDCs were generated from the BM cells of poly(I)•poly(C)-treated *Tln1*$^{f/f}$ and *Tln1*$^{f/f}$*Mx*-Cre mice, as described in Fig. 1 F. Data shown are representative or summaries of three independent experiments. *, 0.01 < P ≤ 0.05; **, 0.005 < P ≤ 0.01 (two-tailed Student's t test).

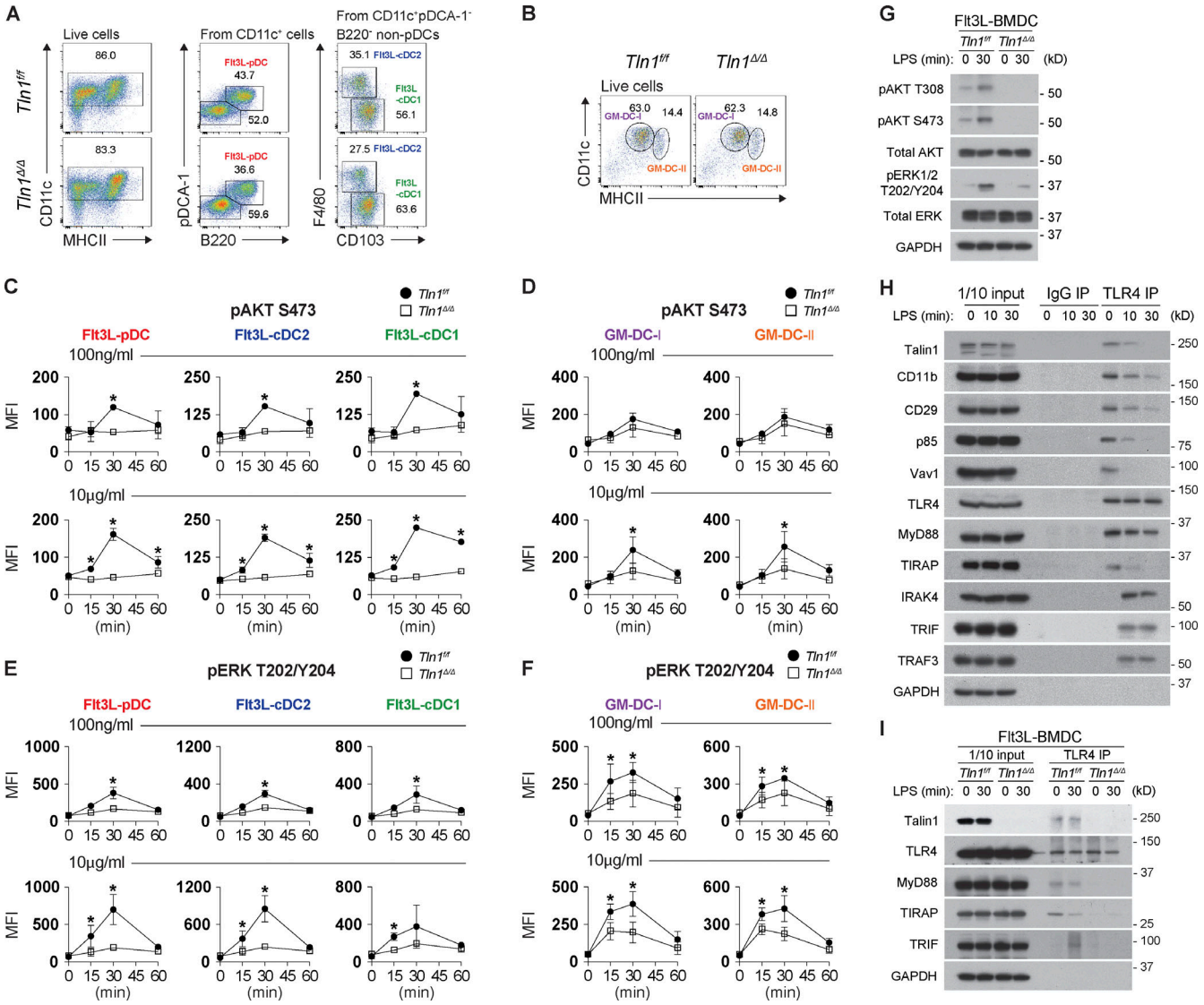

Figure S3. **Talin1 promotes TLR4 signaling in Flt3L and GM-CSF BMDCs. (A and B)** Flow cytometric analysis of wild-type (*Tln1*$^{f/f}$) and talin1-deficient (*Tln1*$^{Δ/Δ}$) BMDCs derived from Flt3L-supplemented (A) or GM-CSF–supplemented (B) cultures. Flt3L-derived BMDCs: pDCA-1$^+$B220$^+$ plasmacytoid DCs (pDC), pDCA-1$^-$B220$^-$F4/80^{hi}CD103^{lo} (cDC2), and pDCA-1$^-$B220$^-$F4/80^{lo}CD103$^+$ (cDC1; A). GM-CSF–derived BMDCs: CD11c$^+$MHCII^{low} (DC-I) and CD11c$^+$MHCII^{high} (DC-II; B). **(C–F)** MFIs summarized from flow cytometric analysis of phospho-AKT S473 (C and D) and phospho-ERK1/2 T202/Y204 (E and F) in BMDC subsets generated from Flt3L-supplemented (C and E) and GM-CSF–supplemented (D and F) cultures stimulated with LPS for the indicated times. **(G)** Immunoblot analysis of wild-type and talin1-deficient Flt3L-BMDCs stimulated with LPS for 30 min. **(H)** IP of TLR4 from total lysates of wild-type GM-CSF-BMDCs stimulated with LPS, followed by immunoblot analysis. IgG is shown as the IP control. **(I)** TLR4 IPs from total lysates of wild-type and talin1-deficient Flt3L-BMDCs stimulated with LPS, followed by immunoblot analysis. IgG is shown as the IP control. GM-CSF-BMDCs or Flt3L-BMDCs were generated from the BM cells of poly(I)•poly(C)-treated *Tln1*$^{f/f}$ and *Tln1*$^{f/f}$*Mx*-Cre mice supplemented with GM-CSF conditioned media (B, D, F, and H) or Flt3L-conditioned media (A, C, E, G, and I). Cells were pooled from two to three mice/group for each IP followed by immunoblot experiment. Data in A–F were pregated on singlet, live CD11c$^+$MHCII$^+$ BMDCs and further dissected into different subsets. Data shown are representative or summaries of three independent experiments (C–F; mean ± SD). *, 0.01 < P ≤ 0.05 (two-tailed Student's *t* test).

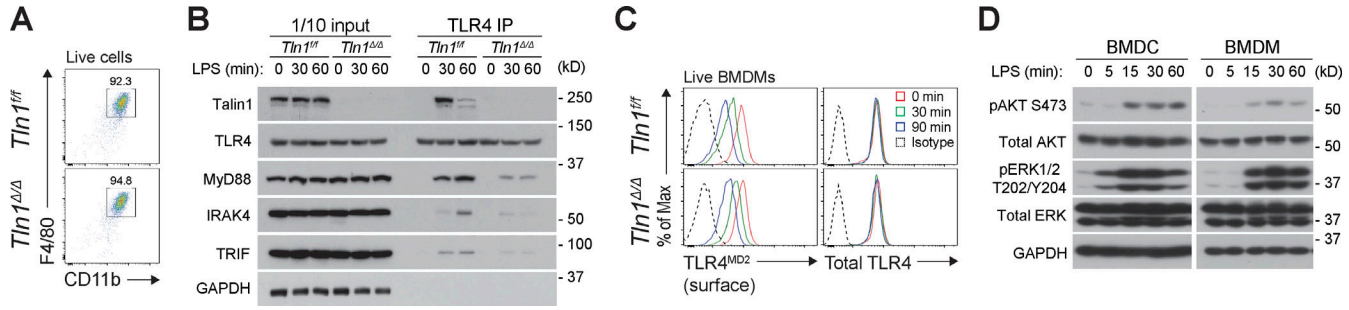

Figure S4. **Talin1 is required for TLR4 signaling in BMDMs without preassembled TLR4 complexes. (A)** Purity of wild-type (*Tln1*$^{f/f}$) and talin1-deficient (*Tln1*$^{Δ/Δ}$) BMDMs used for biochemical analyses. **(B)** TLR4 IP of wild-type and talin1-deficient BMDMs stimulated with LPS, followed by immunoblot analysis. **(C)** Flow cytometric analysis of surface TLR4^{MD2} (left) or total (intracellular and surface) TLR4 (right) of wild-type and talin1-deficient BMDMs stimulated with LPS. **(D)** Immunoblot analysis of wild-type BMDCs and BMDMs stimulated with LPS for the indicated times. Data were pregated on singlet, live F4/80$^+$CD11b$^+$ BMDMs (A and C). BMDMs were generated from the BM cells of poly(I)•poly(C)-treated *Tln1*$^{f/f}$ and *Tln1*$^{f/f}$*Mx*-Cre mice supplemented with conditioned L929 fibroblast cell medium containing M-CSF. BMDMs generated from *Tln1*$^{f/f}$*Mx*-Cre mice are designated as *Tln1*$^{Δ/Δ}$ BMDMs. GM-CSF-BMDCs were generated from the BM cells of poly(I)•poly(C)-treated *Tln1*$^{f/f}$ and *Tln1*$^{f/f}$*Mx*-Cre mice, as described in Fig. 1 F. Cells were pooled from two to three mice/group for each IP followed by immunoblot experiment. Data shown are representative of three independent experiments.

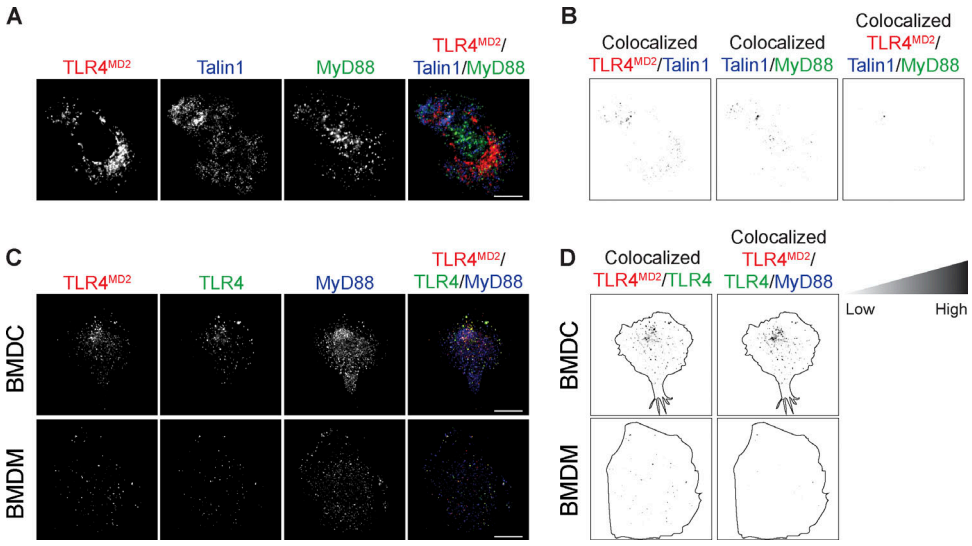

Figure S5. **Preassembled TLR4 complexes are prominent in DCs, not macrophages. (A)** Confocal immunofluorescence microscopy of TLR4^{MD2} (red), MyD88 (green), and talin1 (blue) in wild-type BMDMs. **(B)** Merged images of TLR4^{MD2}/talin1, talin1/MyD88, and talin1/TLR4^{MD2}/MyD88 in wild-type BMDMs. Image intensity corresponds with the degree of colocalization of the indicated molecules. **(C)** Confocal analysis of surface TLR4^{MD2} (red) and TLR4 (green), as well as intracellular MyD88 (blue) in wild-type BMDCs and BMDMs. **(D)** Colocalization analysis of surface TLR4^{MD2}/TLR4 and TLR4^{MD2}/TLR4 with intracellular MyD88 in wild-type BMDCs and BMDMs. Cell outlines are derived from bright-field images of the same cells. Image intensity corresponds with the degree of colocalization of the indicated molecules. Scale bars, 10 µm. BMDMs and BMDCs were generated from the BM cells of poly(I)•poly(C)-treated *Tln1*$^{f/f}$ and *Tln1*$^{f/f}$*Mx*-Cre mice, as described in Fig. S4 and Fig. 1 F. Data shown are representative of three independent experiments (≥10 cells/group pooled from three experiments were inspected).